# Experimental Assessment of Microfluidic Device Performance: Exploring Hydraulic Resistance Across Materials and Geometries for Hemorheology Research

Tatiana Turcitu

A thesis submitted in partial fulfillment of the requirements for the
M.A.SC. in Biomedical Engineering

Ottawa-Carleton Institute of Biomedical Engineering

Faculty of Engineering

University of Ottawa

# Acknowledgement

Firstly, I would like to express my deepest gratitude to my supervisor, Dr. Marianne Fenech, whose guidance, expertise, and unwavering support have been instrumental in the successful completion of this project. Her ability to challenge and inspire me has been a constant source of motivation, and I am incredibly grateful for her willingness to share their knowledge and experience.

Furthermore, I would like to express my sincere gratitude to Dr. Manouk Abkarian from the Centre de Biologie Structurale in Montpellier where I had the opportunity to complete an internship. The experience I gained during my time there has been invaluable, and I am deeply appreciative of the support and guidance. Their expertise and willingness to share their knowledge have been instrumental in my academic growth, and I am grateful for their contribution to this work.

My heartfelt thanks go to my family, especially my parents and my brother, for their unwavering support, patience, and encouragement. They have been my pillars of strength, and without their love and sacrifice, I would not have been able to pursue my academic dreams.

In closing, I would like to acknowledge that this thesis represents not only my own efforts but also the contributions of many individuals who have supported, guided, and inspired me along the way. I am deeply grateful for their support, and I look forward to the opportunity to build on this work in the future.

## Abstract

This project aimed to develop an experimental setup for evaluating the hydraulic resistance and compliance of various microfluidic devices, constructed from different materials (polydimethylsiloxane (PDMS) and Norland Optical Adhesive (NOA)), featuring diverse geometries (tapered-parallel network, hexagonal networks, and retina network), and handling different fluids (water, glycerol, and blood) to optimize microfluidic chip designs for facilitating hemorheology research. The research comprises three main objectives: (1) characterizing the mechanical properties of PDMS and NOA, (2) quantifying compliance under flow rate conditions in microfluidic networks, and (3) analyzing the pressure-flow rate relationship to estimate hydraulic resistance in different geometries. To achieve these objectives, three experimental projects have been performed.

The first project investigates the mechanical and hydraulic properties of tapered-parallel networks fabricated with PDMS and NOA. Results revealed that NOA exhibited a rougher surface, less deformation under pressure, increased hydrophobicity post-plasma treatment, and has a tensile strength 800 times higher compared to PDMS. These mechanical insights offer valuable guidance for material selection to enhance device performance tailored to specific applications. Compliance was computed by measuring the characteristic time of tapered-parallel networks in both NOA and PDMS devices. The analysis demonstrated that NOA microfluidic devices exhibited lower compliance compared to PDMS devices, suggesting potential for improved consistency in microfluidic research. Lastly, the pressure-controlled setup was employed to quantify experimental hydraulic resistance. For tapered-parallel networks, PDMS devices showed higher percentage error in hydraulic resistance due to increased channel deformation and compliance.

The second project evaluates the hydraulic resistance in hexagonal networks under variable red blood cell (RBC) rigidity. An increase of RBC rigidity is associated with an increase in RBC circularity and decrease in deformation. Therefore, the hydraulic resistance will also increase. The results highlight the nuanced interplay between cellular properties and microfluidic resistance, providing a deeper understanding crucial for optimizing microfluidic device performance in hemorheology research.

The third project is collaborative research on the retina network to observe the effect of different fluid viscosities (glycerol and blood) on the hydraulic resistance. In the retina network, resistance increased linearly with glycerol concentration which is typical for Newtonian fluids. In contrast, for blood, the experimental resistance is higher than theoretical values, likely due to uneven distribution of the cells and cell deformability, further highlighting the complex nature of blood flow rate.

Overall, the outcomes enhance understanding of microvascular behavior and facilitate the development of efficient microfluidic devices with applications in biomedical engineering and healthcare.

**Table of Content**

## List of Figures

## List of Tables

## List of Symbols

| | |
|---|---|
| $a$ | Slope |
| $b$ | Intercept |
| $b_1$ | Width entrance of tapered channels [µm] |
| $b_2$ | Width exit of tapered channels [µm] |
| $C$ | Compliance [$\frac{\mu L}{mbar}$] |
| $\Delta$ | Half distance between fibers [µm] |
| $\Delta P$ | Variation of pressure [mbar] |
| $\Delta V$ | Variation of volume [µL] |
| $h$ | Height of channels [µm] |
| $L$ | Length [µm] |
| $\lambda$ | Length of tapered channels [µm] |
| $\mu$ | Viscosity [mPa·s] |
| $p_0$ | Initial pressure [mbar] |
| $Q$ | Flow rate [µL/h] |
| $Q_c$, B | Rate of storage [µL/h] |
| $Q_{in}$, A | Inlet flow rate[µL/h] |
| $Q_{out}$ | Outlet flow rate [µL/h] |
| $R_{chip_{exp}}$ | Chip experimental resistance [$\frac{Pa\cdot s}{m^3}$] |
| $R_{exp}$ | Experimental resistance [$\frac{Pa\cdot s}{m^3}$] |
| $R_{hyd}$ | Hydraulic resistance [$\frac{Pa\cdot s}{m^3}$] |

| | |
|---|---|
| $R_s$ | Peripheral resistance [$\frac{Pa \cdot s}{m^3}$] |
| r | Channel radius [µm] |
| $r_m$ | Radius of micropillars [µm] |
| $t$ | Time [s] |
| $\tau$, D | Characteristic time [s] |
| w | Width of channel [µm] |

# List of Acronyms

| | |
|---|---|
| ATP | Adenosine triphosphate |
| EI | Elongation Index |
| $EI_{max}$ | Elongation Index max |
| HCT | Hematocrit |
| LDPI | Laser Doppler Perfusion Imaging |
| LSCI | Laser Speckle Contrast Imaging |
| NOA | Norland Optical Adhesive |
| OCT | Optical Coherence Tomography |
| PBS | Phosphate Buffered Saline |
| PVP | Polyvinylpyrrolidone |
| PDMS | Polydimethylsiloxane |
| RBC | Red Blood Cells |
| SS | Shear Stress |
| $SS_{1/2}$ | Half Shear Stress |
| UV | Ultraviolet |
| WBC | White Blood Cells |

# 1 Introduction

## 1.1 Research Motivation

Microfluidics has emerged as a promising technology for various applications, including chemical synthesis, drug delivery, biological analysis, and lab-on-a-chip devices [1], [2]. The behaviour of complex fluids at the microscale is fundamentally different from that at the macroscale, and understanding the relationship between pressure, flow, resistance, and compliance is crucial for the successful design and operation of microfluidic devices [3], [4].

Pressure (the force exerted by a fluid per unit area) and flow (the movement of fluid from one point to another) are critical parameters that describe the behaviour of fluids in microchannels. Measuring them accurately is necessary for optimizing the performance of microfluidic systems [5]. On the other hand, resistance (defined as the opposition to flow) and compliance (the measure of a system's ability to expand in response to pressure) are properties of microchannels that affect the flow of fluids and the distribution of pressure within the system [6]. The ability to control and manipulate these parameters can enable new applications and improve the reliability and reproducibility of microfluidic devices [6].

Although significant progress has been made in recent years, there are still many challenges and open research questions related to pressure, flow, resistance, and compliance in microfluidics [6], particularly in the context of micro blood flows. These challenges include understanding the impact of complex blood composition and cell deformability on flow behavior, as well as the development of accurate and reliable experimental and computational methods for characterizing microfluidic systems. For example, the development of new materials and fabrication techniques for microfluidic devices with tunable resistance and compliance could enable new applications in biomedical engineering, such as organs-on-chips or drug delivery systems [6].

Hemorheology is the study of blood flow and its impact on the microcirculation. It is important for understanding various diseases such as cardiovascular diseases (myocardial infarction, hypertension), metabolic conditions (diabetes, obesity), and hematological disorders (plasma cell dyscrasia, sickle cell disease) [7]. To study blood flow, it is essential to characterize its non-Newtonian behaviour in capillaries, where its viscosity varies with the size of blood vessels and is influenced by factors such as the hematocrit, red blood cell (RBC) deformation, RBC aggregation, and the resistance and compliance of blood vessels [8]. Furthermore, understanding red blood cell behaviour can aid in optimizing drug delivery and medical diagnostics [9]. This research is motivated by the need to address these challenges and further advance microfluidic technology and hemorheology research.

## 1.2 Background Research

This section provides an overview of microfluidics, including the Hagen-Poiseuille flow model, resistance and compliance, the effect of channel dimensions, microfabrication methods, and different microfluidic devices materials. This section also discusses the importance of understanding blood composition and microcirculation for biomedical applications. Plus, a review of the hemorheological properties of blood will be presented.

### 1.2.1 Microfluidics in Biomedical Applications: Design, Fabrication, and Characterization

Pressure, flow, resistance, and compliance are interconnected parameters that affect the performance of microfluidic devices. They play a critical role in understanding and controlling fluid behaviour. By adjusting these parameters, the flow rate, direction, and volume of fluids in the microchannels can be measured and manipulated [3]. These parameters can optimize microfluidic devices design, detect abnormalities (blockage and leakage of the device) and mimic physiological conditions. These are particularly important in biomedical applications such as chemical synthesis, biological assays, and lab-on-a-chip devices where precise control of fluid flow is necessary [1], [2]. For these reasons, the pressure-flow rate relation, the resistance and compliance will be further explained in this section.

In biomedical applications, the material used to fabricate the microfluidic devices must be hydrophilic, biocompatible, low cost, transparent, and easy and fast to manufacture [1], [10], [11]. To optimize the microfluidic device, the fabrication process and the material used must correspond to the application. For these reasons, microfabrication processes will be further presented as well as material consideration for biomedical applications.

#### *1.2.1.1 Pressure-Flow Rate Relation*

The Hagen-Poiseuille equation describes the laminar flow of a Newtonian fluid through a long, straight and rigid channel with constant cross-sectional area, imposing a pressure difference along the channel [12]. According to the Hagen-Poiseuille equation, the pressure difference ($\Delta P$) is directly proportional to the volumetric flow rate (Q) and the hydraulic resistance ($R_{hyd}$) of the channel (defined as opposition to flow). Mathematically, this can be expressed as [12]:

$$\Delta P = QR_{hyd} \qquad \text{Equation 1}$$

where $\Delta P$ is the difference of pressure across the channel, $Q$ is the flow rate and $R_{hyd}$ is the hydraulic resistance. In this model, the flow is assumed to be laminar, steady, fully developed, and the fluid incompressible and Newtonian [4], [12], [13]. At low Reynolds numbers, such as the ones in this research (Re < 20), fluid flow is governed by the Hagen-Poiseuille model.

The theoretical hydraulic resistance of multi-channels microfluidic devices are computed by combining the individual resistances in series or parallel as with electrical circuits using the following equations [13]:

$$R_{eq_{series}} = R_{hyd_1} + R_{hyd_2} + \cdots + R_{hyd_n} \qquad \text{Equation 2}$$

$$R_{eq_{parallel}}{}^{-1} = R_{hyd_1}{}^{-1} + R_{hyd_2}{}^{-1} + \cdots + R_{hyd_n}{}^{-1} \qquad \text{Equation 3}$$

The hydraulic resistance of the rectangular cross-section channels can be calculated using the Hagen–Poiseuille equation as follows [13]:

$$\mathrm{R_{hyd}} = \frac{12\,\mu L}{d_1 d_2^3 (1 - \frac{0.63 d_2}{d_1})} \qquad \text{Equation 4}$$

where $d_1$ is length of the rectangular cross-section's shorter edge, $d_2$ length of the rectangular cross-section's longer edge, µ is the viscosity of the fluid, and $L$ is the length of the channel in question. The hydrodynamic resistance of the tapered channels can be calculated using the Darcy law, as follows [13]:

$$R_{hyd} = \frac{9\lambda\pi\mu\sqrt{2}}{8 r_m^2 h \left(\frac{\Delta}{r}\right)^{5/2} (b_1 + b_2)} \qquad \text{Equation 5}$$

where $b_1$ is the width of entrance, $b_2$ the width of exit, h the height of the channel, r the radius of the micropillar, $\lambda$ the length of the tapered channels and $\Delta$ the half distance between fibers. The hydraulic resistance of circular channels can be calculated using the Hagen-Poiseuille equation ad follows:

$$R_{hyd} = \frac{8\mu L}{\pi r^4} \qquad \text{Equation 6}$$

where μ is the viscosity of the fluid, $L$ is the length of the channel, and $r$ is the radius of the channel in question. The table below summarizes the different shapes and resistances of the channels.

**Table 1: Summary of the different shapes and hydraulic resistances.**

<table>
<tr><th>Shape</th><th>Hydraulic Resistance</th></tr>
<tr><td>Rectangular
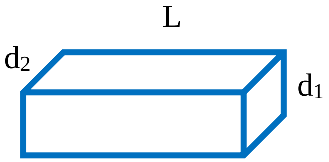

where $d_2 \ll d_1$</td><td>$$R_{hyd} = \frac{12\,\mu L}{d_1 d_2^3 (1 - \frac{0.63 d_2}{d_1})}$$</td></tr>
<tr><td>Tapered channels with micropillars
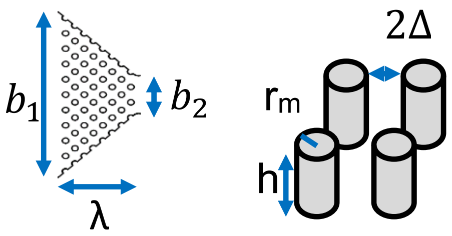
</td><td>$$R_{hyd} = \frac{9\lambda\pi\mu\sqrt{2}}{8 r_m^2 h \left(\frac{\Delta}{r}\right)^{5/2} (b_1 + b_2)}$$</td></tr>
<tr><td>Circular
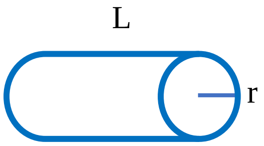
</td><td>$$R_{hyd} = \frac{8\mu L}{\pi r^4}$$</td></tr>
</table>

### *1.2.1.2 Resistance and Compliance*

Resistance and compliance are key parameters in microfluidic design system. Resistance is the opposition to flow and is defined by the change in pressure over volumetric flow rate ($R=\Delta P/Q$). The hydraulic resistance is determined by the channel geometry which is a function to the power of 4 of the channel diameter [10], [14]. The hydraulic resistance is also determined by the fluid properties. Compliance is the measure of the channel elasticity and defined by the change in relative volume over the change in pressure ($C=\Delta V/\Delta P$).

##### *1.2.1.2.1 Effect of Channel Dimensions*

The hydraulic resistance, compliance and shear are influenced by the channel's dimensions. As discussed previously, the fluid flow rate is governed by the Hagen-Poiseuille model where the hydraulic resistance is dependent on the dimensions of the channel. Therefore, a small variation in the channel dimensions due to deformation can significantly change the resistance. To overcome the system resistance, a high pressure (hundreds of bars) can be required. This will significantly change the channel dimensions. Under pressure, the compliance (change in volume for any given pressure) will impact the channel dimensions [10], [15]. By measuring the time required to reach steady state conditions (also called response time and characteristic time) with a syringe pump, the compliance can be calculated. The characteristic time can vary from seconds to hours depending on the hydraulic resistance and compliance [4], [10]. Hence, an accurate measurement of the channel dimensions is crucial in microfluidics. In microrheology studies, the channel dimensions directly influence the development of viscosity laws and the understanding of the relationships between shear forces and microstructures [16], [17], [18].

Also, the dimensions of microfluidic channels directly influence fluid behaviour, including flow rate, pressure drop, mixing, and diffusion [4]. Any variation in channel dimensions can lead to inconsistent results and unreliable experimental outcomes. By precisely controlling the dimensions, researchers can manipulate the flow rate and achieve desired fluid velocities [19]. This is crucial for applications such as drug delivery, where precise control of flow rate is necessary to ensure accurate dosing. Similarly, in biological applications, such as cell culture and analysis, constant channel dimensions allow for consistent fluid flow rate and controlled interactions between cells and reagents [20]. To ensure optimal channel dimension, the microfabrication process and material of the microfluidic device must be carefully selected.

#### *1.2.1.3 Microfabrication Methods*

The main focus of this section will be on photolithography and soft lithography since they are part of the most important microfabrication techniques in microfluidics [21].

Photolithography is a technique used to create patterns on a photomask. The process involves several steps, including coating the substrate with a light-sensitive material called photoresist, exposing the photoresist to ultraviolet (UV) light through a photomask, and developing the photoresist to create a patterned layer [22]. The patterned layer can then be used as a template for subsequent processing steps, such as etching or deposition. SU-8 wafers are commoly used as phtotoresist in microfluidics [2]. Photolithography is a highly precise and versatile technique that can produce features ranging in size from microns to nanometers in materials such as silicon, glass, and light sensitive polymers [11], [21]. It is widely used in the fabrication of integrated circuits, microelectromechanical systems (MEMS), and microfluidic devices [22].

Soft lithography is a replication-based method. This means that a master (also called a mold) is crucial to the fabrication process [22] [11]. The master can be fabricated using conventional photolithography, silicon etching and many more [11]. When the mold is created using conventional photolithography, a silicon wafer is used which is then replicated with PDMS and bonded to a substrate. Soft lithography offers advantages such as versatility, cost-effectiveness, and biocompatibility [11], [21]. It enables precise control over microstructure geometry and dimensions and facilitates rapid prototyping for iterative design processes [11], [21]. Applications span biomedical research, chemical analysis, diagnostics, and biotechnology, including cell culture, drug screening, and portable diagnostic devices [11], [21].

### *1.2.1.3.1 Material consideration*

To optimize microfluidic devices in biomedical applications, the material used to fabricate the microfluidic devices must be hydrophilic, biocompatible, low cost, transparent, and easy and fast to manufacture [1], [10], [11]. Multiple materials have been used to fabricate microfluidic chips and are classified into the following categories: glass, silicon, polymeric (siloxane elastomers, thermosetting polymers and thermoplastic polymers) and adhesives (pressure sensitive and optical) [11]. Glass and silicone have been used due to their resistance, stiffness, and durability, but their high cost led to the investigation of other materials for microfluidic devices [11]. Polymers have been used mostly in academic research due to their biocompatibility, transparency, mechanical (elastic or stiff) and chemical properties and low cost [11]. Adhesives present the cheapest, easiest and fastest way to fabricate microfluidic devices, can be transparent and are also biocompatible [11]. Their investigation is required to offer critical guidance to researchers in selecting the most suitable materials for their specific application. The next sections will discuss microfluidics devices made of polymer (polydimethylsiloxane (PDMS) which is the predominant material in the field and an optical adhesive (Norland Optical Adhesive (NOA)) to show the differences between these materials.

#### 1.2.1.3.1.1 Polydimethylsiloxane devices

Microfluidic devices are predominantly fabricated using PDMS because of its transparency [23], low cost, and ease of manufacturing [10], [24], [25], [26]. PDMS has a low elastic modulus (1 to 3 MPa), allowing the device to deform under high pressure [25], [26], [27]. This can significantly change the channel dimensions and therefore affect the resistance, compliance and shear estimation. The investigation of a rigid material than can overcome the limitations associated with PDMS is important for studies that require high pressure.

#### 1.2.1.3.1.2 Norland Optical Adhesive devices

NOA can be used instead of PDMS to manufacture microfluidic devices. NOA offers more rigidity and is less compliant. This material is clear and has a high Young modulus (1655 MPa) [28]. This allows NOA to be used in high-pressure flow systems with minimal compliance. This has been shown by Elodie Sollier et al. when comparing, in high-pressure flow systems, PDMS to other forms of polymer-based materials like NOA, [10], [29]. Their findings revealed that the maximum pressure ($P_{max}$) at which delamination occurs in NOA is approximately 74–79 PSI, while PDMS bonded to glass experienced delamination at pressures as low as 36 PSI [29]. NOA is a material that needs to be further explored to determine its potential for biomedical applications such as microcirculation.

## 1.2.2 Physiology of Microcirculation

The composition of blood, including plasma and its solutes, plays a critical role in maintaining the body's functions. Understanding blood composition and microcirculation is essential for biomedical applications, medical diagnostics, and the study of diseases such as cardiovascular and metabolic conditions.

### *1.2.2.1 Blood Composition*

Blood is composed of plasma, white blood cells (WBC) and platelets, and red blood cells (RBC). Plasma, with its yellowish color, represents about 55% of the volume of a blood sample. It consists of 90% water and 10% solutes. The various solutes present are electrolytes that maintain the osmotic pressure of the plasma and the blood pH. Plasma proteins contribute to maintaining osmotic pressure, the water balance of blood and tissues, transport nutrients and metabolic wastes, aid in the body's defense, participate in coagulation, and transport hormones from endocrine glands [30].

White blood cells and platelets represent less than 1% of the volume of a blood sample and form a whitish layer between the plasma and red blood cells [30]. White blood cells are a defense mechanism of the body. They are the only nucleated cells in the blood. The two types of white blood cells are granulocytes, which are spherical in shape and have a diameter of 10 to 14 µm, and agranulocytes, which are spherical in shape and have a diameter of 5 to 24 µm [30]. Platelets are discoid cell fragments measuring 2 to 4 µm. Their function is to participate in blood clotting [30].

The density of blood is 1060 kg/m$^3$. Plasma density is 1030 kg/m3, and red blood cell density is 1100 kg/m$^3$. Red blood cells represent in average 40-45% of the total volume of a blood sample. This percentage is also called hematocrit [30], [31].

The function of red blood cells (RBC), also called erythrocytes, is to transport respiratory gases ($O_2$ and $CO_2$). Erythrocytes capture oxygen in the capillaries of the lungs and transport it to the cells of the tissues via the capillaries. Red blood cells also transport 20% of $CO_2$ to the lungs. Erythrocytes are small, anucleated cells with biconcave shapes measuring 7 to 8 µm in diameter and 2 µm in height, with a center measuring 1 µm (Figure 1) [31]. Red blood cells maintain their biconcave shape thanks to a network of fibrous proteins, including spectrin. Spectrin is deformable, giving red blood cells the flexibility they need to twist, bend, and indent as they pass through capillaries [30], [31].

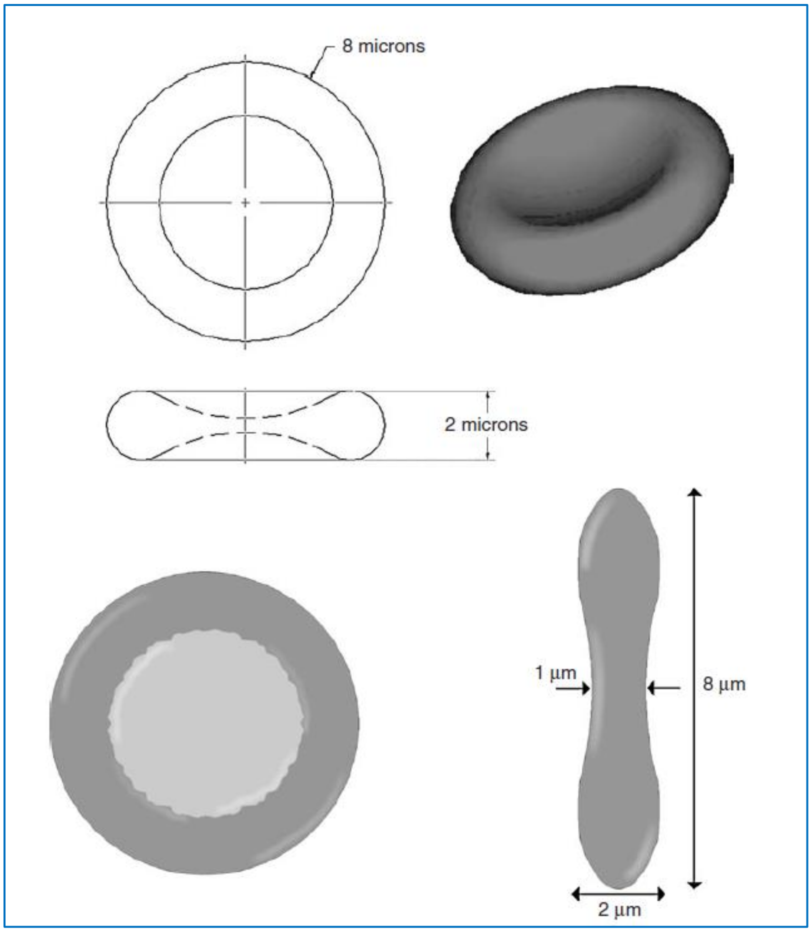

**Figure 1: Shape and dimensions of RBC [31].**

### *1.2.2.2 Microcirculation*

Microcirculation comprises the end of the vascular network within the systemic circulation, encompassing tiny vessels (less than 20 µm), namely arterioles, venules, and capillaries (Figure 2) [32]. The systemic pressure in these vessels is between 5-80 mmHg (7-107 mbar) [33]. The microcirculation is responsible for the oxygen transport from the red blood cells in the capillaries to the parenchymal cells to support organ function [30], [32]. It is also responsible for the solute exchange between intravascular and tissue spaces to facilitate hormone and nutrient transport [30], [32]. It plays a pivotal role in modulating immune system function and hemostasis [32].

Understanding the functioning of the microcirculation is important for studying cardiovascular (hypertension, stenosis), metabolic (diabetes), and hematological (sickle cell disease) diseases as well as developing therapeutic solutions. To better study microcirculation, it is important to understand the morphology of capillaries. To do so, imaging of the microcirculation is needed. Three techniques can be used: videomicroscopy, laser doppler perfusion imaging (LDPI) and laser speckle contrast imaging (LSCI) [34]. Videomicroscopy can measure the vessel diameter and density, the RBC velocity and heterogeneity [34]. It has direct visualization of the microcirculation. Videomicroscopy presents some disadvantages including motion and pressure artifacts and the analysis is time consuming [34], [35]. This technique is mostly used to study the sublingual mucosa in patients with sepsis (improper body response to infection) [34]. LDPI can measure the RBC mean velocity and concentration with no contact [34]. Its disadvantages are motion artifacts, low resolution, long measurement time and relative measurements. It is mostly used in dermatology for the differentiation of skin lesions [34]. LSCI can measure the RBC mean velocity and concentration with no contact [34]. Its disadvantages are motion artifacts, low resolution and relative measurements [34], [35]. It is mostly used for functional test of skin microcirculation [34]. These non-invasive methods for studying microcirculation *in vivo* are limited and do not generate high-resolution images [35]. Consequently, investigating capillary cardiovascular pathologies is challenging. However, optical coherence tomography (OCT) enables a unique, non-invasive, *in vivo* study of blood vessels in the human retina with high resolution [36]. This technology can be used to visualize blood vessels to replicate them *in vitro*, facilitating the study of microcirculation for the development of treatments for microcirculation-related diseases. The retinal microcirculation and its applications are discussed in Section 1.2.2.3.

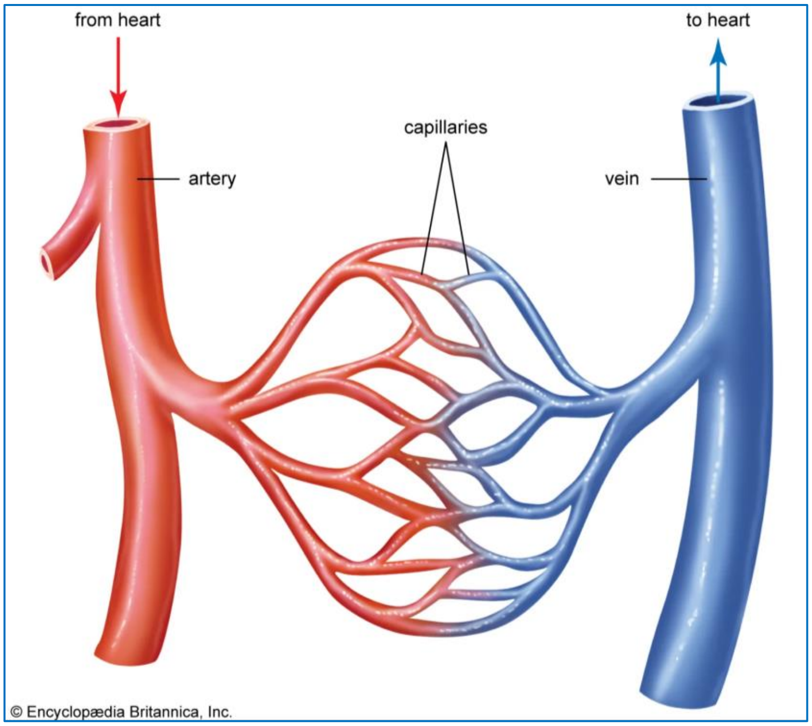

**Figure 2: Capillary beds [37].**

#### *1.2.2.3 Retinal Microcirculation*

As mentioned previously, the retina offers a unique way to study microcirculation. The retinal microvascular network may undergo hemodynamic and morphological disturbances, affecting blood flow distribution and tissue oxygenation [38]. These alterations may also indicate blood circulation problems throughout the body due to cardiovascular diseases such as hypertension and diabetes, as well as several neurodegenerative diseases such as Alzheimer's, Parkinson's, and Huntington's [39], [40]. Hypertension is also the cause of several retinal abnormalities such as generalized arteriolar narrowing, focal arteriolar narrowing, arteriovenous nicking, and retinopathy [41]. Additionally, the retinal network can be used to better understand and find treatment for central retinal vein occlusion, which causes vision loss [42]. Moreover, the retinal network can be used to better understand microcirculation in the brain to treat strokes. Due to all these microcirculation-associated diseases that can be determined by the retinal network, it is interesting and important to create an in vitro model to study and better understand the mechanism and functioning of retinal microcirculation related to these diseases.

### 1.2.3 Hemorheology

The study of blood flow and its impact on microcirculation, known as hemorheology, holds significant importance in understanding various diseases such as cardiovascular diseases, metabolic conditions, and hematological disorders. Hemorheology explores the non-Newtonian characteristics of blood, which are shaped by elements such as the resistance and flexibility of blood vessels, viscosity that is associated with hematocrit, red blood cell deformability, aggregation, and cell migration.

#### *1.2.3.1 Viscosity*

Viscosity is a measure of the fluid’s resistance to deformation of the fluid element under shear. In this thesis, the focus is on the fluid's dynamic viscosity, which is defined as the ratio of shear stress to shear rate [43]. The common unit for dynamic viscosity is Poise (P) [43]. Figure 3 represents the shear stress as a function of shear rate for Newtonian and non-Newtonian fluids. In the case of non-Newtonian fluids, the shear stress is not proportional to the shear rate creating shear-thinning fluids and shear-thickening fluids. For shear-thinning fluids the viscosity decreases as shear rate increases meaning that it flows more easily and exhibits lower resistance to flow as the shear rate increases [2], [43]. Examples of shear-thinning fluids are ketchup and blood [2], [43]. For shear-thickening fluids, viscosity increases as shear rate increases meaning that it becomes more resistant to flow and exhibits higher viscosity as the shear rate increases [2], [43]. Example of shear-thickening fluid is water-sand mixture [2], [43].

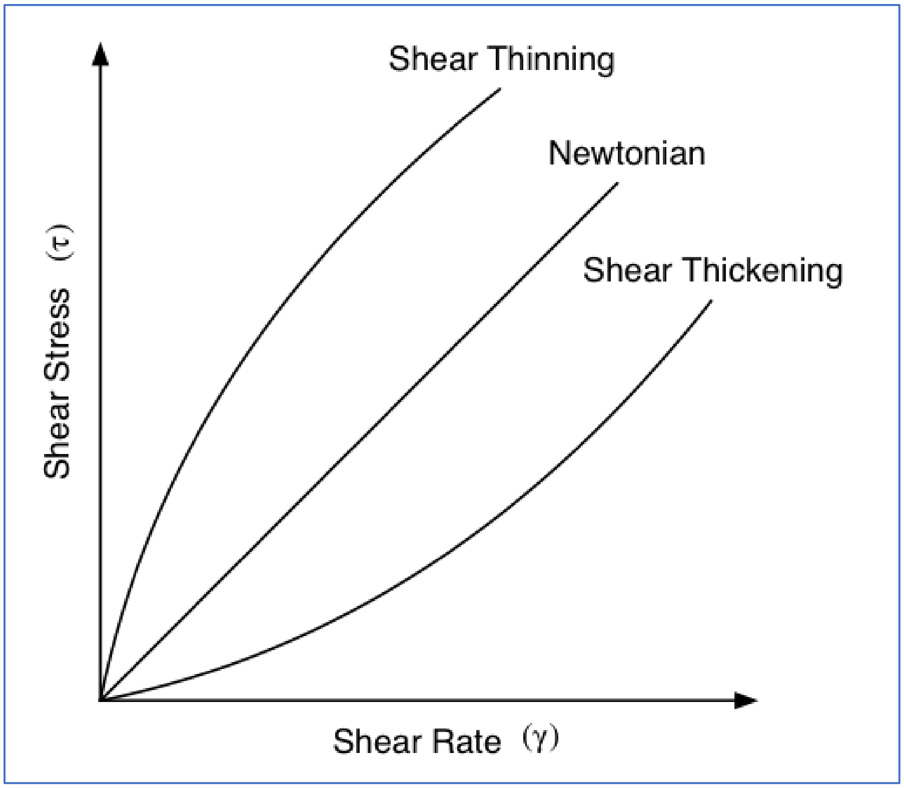

**Figure 3: Representation of shear stress as a function of shear rate for Newtonian and non-Newtonian fluids [44].**

As mentioned previously, blood is non-Newtonian. Figure 4 shows that blood viscosity decreases with increasing shear rate. Indeed, viscosity changes depending on hemodynamic properties. This means that viscosity varies in different blood vessels (arteries, capillaries, veins). Blood viscosity depends on several factors such as hematocrit, plasma viscosity, red blood cell deformation, erythrocyte aggregation, and the development of the cell-depleted layer [8]. These various factors are important for a better understanding of blood behaviour in the human body. For this reason, they will be explained in the following sections.

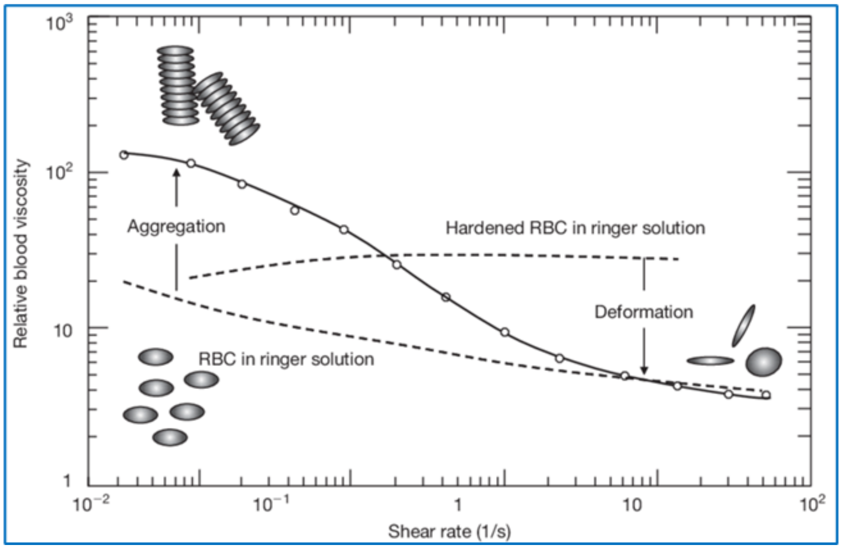

**Figure 4: Relative blood viscosity as a function of the shear rate [45].**

### *1.2.3.2 RBC Deformation*

Red blood cells must deform to pass through capillaries that have a smaller diameter than that of erythrocytes. The deformability of red blood cells is made possible by spectrin. Spectrin provides the strength and elasticity necessary for the membrane to deform, giving it viscoelastic properties [46]. The deformation of red blood cells is very important as it helps to reduce resistance in blood vessels and thus facilitates the transport of oxygen and ATP (adenosine triphosphate), which is the stored energy source used in cells [30], [46], [47], [48].

Red blood cells deform into different shapes. Figure 5 compares the normal shape of red blood cells (a) to an asymmetric shape (b) and to the parachute shape (c) [48]. Parachute-shaped erythrocytes are axisymmetric. The shape of red blood cells changes depending on shear. Indeed, at higher flow rates or in capillaries with diameters smaller than the size of red blood cells, they tend to deform into a parachute shape as shown in Figure 5 (c). Whereas red blood cells in asymmetric shape deform in this way at lower flow rates (Figure 5 (b)). Additionally, the deformation of erythrocytes depends on the viscosity of the suspension. Increasing suspension viscosity increases red blood cell deformation and consequently decreases shear rate [48], [49].

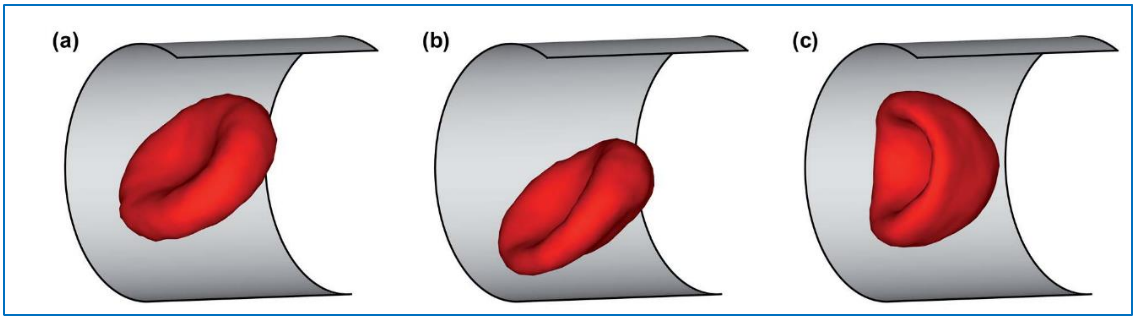

**Figure 5: Different shapes of red blood cells (a) normal, (b) asymmetric and (c) parachute [48].**

Several diseases affect the deformation of red blood cells, such as diabetes and sickle cell anemia. Diabetics have higher blood viscosity than non-diabetics, leading to poorly oxygenated tissues. Also, the biconcave shape of red blood cells is elongated in patients affected by diabetes [50].

Sphericity is an important morphological parameter for RBCs because it provides insights into their health and functionality. Hereditary spherocytosis is a hematologic disease characterized by spherical cell due to the loss of membrane area relative to volume [51]. This abnormal shape has been found to affect the ability of the RBCs to deform which is essential for passing through the capillaries [51]. Less deformation of the RBCs signifies a rigidified membrane.

The standard method for estimating the deformation of red blood cells is ektacytometry, which utilizes laser diffraction to measure changes in cell shape. An RBC suspension is created using a small amount of blood in a viscous solution of a certain osmolarity. Depending on the device used, the RBC suspension can be placed in between two coaxial cups (one fixed and one that rotates) (for example the Lorrca device) or in a microfluidic chip (for example the RheoScan device) (see Figure 6) [52], [53], [54]. The RBC are deformed by the rotation of the cup which creates a shear stress (Lorrca) or by a pump that applies a shear stress (RheoScan). For these methods, the RBC suspension is illuminated with a laser beam and a diffraction pattern appears on the computer software as well as the dynamics [54]. The shape of the pattern is circular or elliptic depending on the deformation of RBC due to the applied shear stress. An elliptic shape means that the RBCs are more deformable while a circular shape means that they are less deformable.

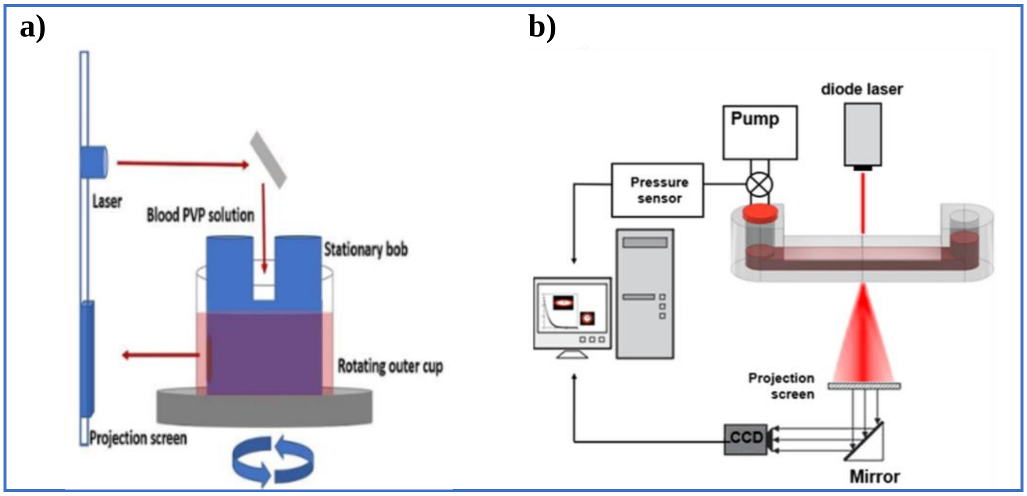

**Figure 6: Representation of the ektacytometry technique for a) two coaxial cups (Lorrca device) [53] and b) microfluidic chip (RheoScan device) [52].**

For *in vitro* studies, RBC can be chemically modified to rigidify the cell membrane. By rigidifying the cell membrane, the RBC will deform less. There are two common chemicals used to study the rigidity of the RBCs: diamide and glutaraldehyde. Diamide is a sulfhydryl oxidant that increases protein-protein associations with induced formation of inter- and intra- disulfide bonds which increases the rigidity of the RBC’s membrane [55]. Glutaraldehyde is an organic compound that crosslinks proteins and therefore rigidifies the RBC’s membrane. It increases the shear modulus and viscosity of the cells which increases the rigidity of the RBCs.

### *1.2.3.3 RBC Aggregation*

Aggregation occurs under low shear stress and is characterized by the clustering of red blood cells on top of each other to create rolls (Figure 7). The rolls can form structures in 2 dimensions or 3 dimensions [7]. Aggregation decreases with increasing shear rate. Aggregation is a reversible process when the shear stress exceeds approximately 100 $s^{-1}$ [7].

**Figure 7: Rolls formed by the aggregation of RBC [7].**

Several factors affect the aggregation of red blood cells. An increase in aggregation size is observed with an increase in hematocrit [56]. Another aspect affecting aggregation is the concentration of macromolecules in the plasma. As the concentration of macromolecules increases, the size of the aggregation also increases. Additionally, a decrease in red blood cell surface charge density (amount of charge per unit surface area) promotes an increase in aggregation size [57]. Finally, the less deformable erythrocytes are, the less aggregation occurs [7], [57]. The aggregation level of red blood cells is often increased in several medical conditions such as infections, cardiovascular diseases, metabolic diseases, and hematological diseases [7].

#### *1.2.3.4 Cell-Free Layer*

The cell-free layer, also known as the cell-depleted layer, is a layer of plasma near the walls of a blood vessel without red blood cells (Figure 8) [58]. This layer acts as a lubricating layer because it has a lower viscosity than red blood cells, which helps reduce the effective viscosity of blood [58]. The Fahraeus-Lindqvist effect is a phenomenon that corresponds to the decrease in apparent blood viscosity for a decreasing tube diameter [58]. This effect is due to the creation of two phases during the migration of red blood cells. The first phase is characterized by red blood cells moving into the center of the tube, known as the core [58]. The second phase is the cell-free layer, which plays a crucial role in reducing the overall resistance to blood flow in small blood vessels.

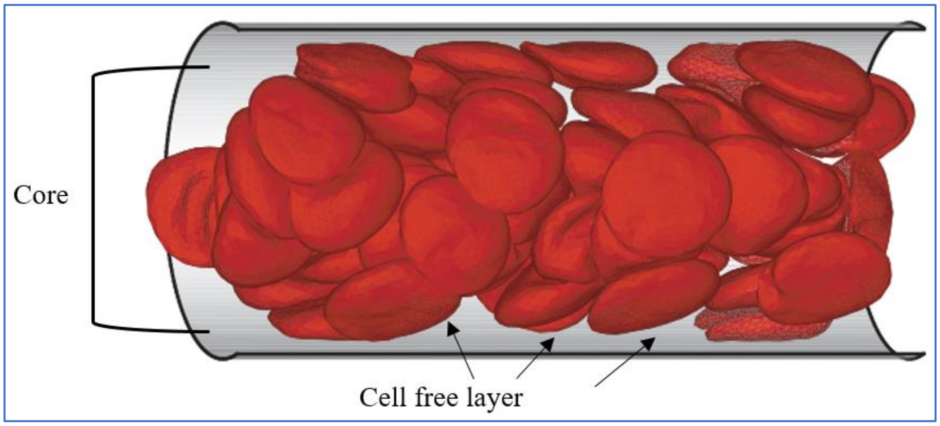

**Figure 8: Representation of the Fahraeus-Lindqvist effect [58]**

The thickness of the cell-depleted layer depends, among other factors, on volumetric flow rate, hematocrit, and red blood cell aggregation [9]. Several studies have demonstrated that the cell-depleted layer has a greater thickness for lower hematocrits and depends on the diameter of the tube. In tubes with small diameters (less than 100 μm) and high hematocrits, the thickness of the cell-depleted layer can significantly change the apparent viscosity. Additionally, the thickness of the cell-depleted layer decreases with increasing shear stress or flow rate [58].

#### *1.2.3.5 Resistance and Compliance*

Peripheral vascular resistance is a crucial factor in determining blood pressure and flow rate in the circulatory system. It is influenced by the contraction and relaxation of blood vessels, with resistance increasing during vasoconstriction and decreasing during vasodilation [59]. The formula for calculating resistance is defined as the change in pressure over the volumetric flow rate (R=ΔP/Q) [13]. Arterioles are the primary site of vascular resistance, with a resistance value of 13 mmHg/L/min, while capillaries have a lower resistance of 5 mmHg/L/min. These values are based on a normal, young adult of 70 kg [60]. Clinical conditions such as hypertension and hypotension are often associated with abnormal peripheral vascular resistance [59].

Compliance, on the other hand, is a measure of the elasticity of blood vessels. It is defined as the change in relative volume over the change in pressure (C=ΔV/ΔP) [61]. In a normal, young adult of 70 kg, the compliance of arterioles and capillaries is negligeable [60]. However, the venous system and the ventricle in diastole have higher compliance values, ranging from 4-110 ml/mmHg and 24 ml/mmHg, respectively [60]. A decrease in compliance, which is equivalent to an increase in vessel stiffness, can significantly impact blood pressure and blood flow [61].

## 1.3 Research Statement and Objectives

This project aims to establish an experimental framework for evaluating the hydraulic resistance of various microfluidic devices, each fabricated from different materials (PDMS and NOA), geometries (tapered-parallel, hexagonal, and retina networks), and fluids (water, glycerol, and blood). The ultimate goal is to optimize microfluidic chip designs and contribute to hemorheology research.

To accomplish this, key objectives must be met:

1. A comprehensive investigation into the mechanical properties of PDMS and NOA, two materials used for microfluidic device fabrication. This includes characterizing surface roughness, tensile strength, channel width deformation, and contact angle.
2. Quantifying the compliance under flow rate for networks in both NOA and PDMS devices.

3. Examining the pressure-flow rate relationship of the different networks (tapered-parallel, hexagonal, and retina) to estimate and interpret the hydraulic resistance of the microfluidic devices for various fluids (water, glycerol, and blood).

It's important to note that the knowledge gained from the compliance chip investigation for the second objective allows us to evaluate in which regime the non-linearity arises, whether it's from the compliance or the fluid properties. The third objective is to examine the pressure-flow rate relationship of the different networks (tapered-parallel, hexagonal, and retina) to estimate the hydraulic resistance of the microfluidic devices for various fluids (water, glycerol, and blood). In this context, the pressure-flow rate relationship can exhibit non-linear behavior due to the compliance of the device or the properties of the fluid being used. By combining the insights from the second and third objectives, we can assess the non-linearity in the pressure-flow rate relationship and identify whether it's primarily caused by the device's compliance or the fluid's properties. This understanding will contribute to the optimization of microfluidic chip designs and the advancement of hemorheology research.

Ultimately, the outcomes of this research will not only enhance our understanding of fluid flow control and microvascular behaviour but also contribute to the development of more efficient, reliable, and cost-effective microfluidic devices with broad implications in biomedical engineering, healthcare, and beyond.

## 1.4 Overview of the Three Experimental Projects Undertaken During the Master's Thesis

To contribute to the main goals presented above, three experimental projects have been performed targeting microfluidic and hemorheology research.

### 1.4.1 Investigation of Mechanical and Hydraulic Properties of Tapered-Parallel Networks

The first project uses three tapered-parallel networks designed by Niko Lee-Yow at the University of Ottawa. In this research, I used three different tapered-parallel networks of various dimensions and fabricated them with different materials, NOA and PDMS (6 devices in total). The mechanical properties (surface roughness, tensile strength, contact angle and channels deformation) of NOA and PDMS were investigated to achieve the first objective mentioned in the previous section. Then, the compliance of the six devices was quantified using a syringe pump setup to reach the second objective. Lastly, the hydraulic resistance of the 6 devices was estimated for water as the fluid under pressure-flow rate control to complete the third objective. The results of this project were published in Micromachine and presented at the FFHMT2023 conference.

- *Turcitu T. Armstrong C.J.K Lee-Yow N. Salame M. Le A.V. Fenech M. Comparison of PDMS and NOA Microfluidic Chips: Deformation, Roughness, Hydrophilicity and Flow Performance. Micromachine, 2023, 14(11), 2033; https://doi.org/10.3390/mi14112033*
- *Turcitu T. Armstrong C.J.K. Lee-Yow N. Le A.V. Fenech M. Comparison of the Compliance and Deformation Properties of PDMS and NOA Microfluidic Chips Proceedings of the 10th International Conference on Fluid Flow, Heat and Mass Transfer (FFHMT 2023), 178, DOI: 10.11159/ffhmt23.178*

### 1.4.2 Evaluation of Hydraulic Resistance in Hexagonal Networks under Variable RBC Rigidity

The second project presents my contribution to a collaborative work with Dr. Abkarian's research group, where I completed a 3-month internship. This project explores the microhemodynamics of blood in networks, linking local measurements such as red blood cell shape in the network to macroscopic measurements such as pressure-flow rate behavior. My specific contribution was to conduct the experiment and to analyze the hydraulic resistance of the four hexagonal networks perfused with blood suspensions of different rigidity, while the PhD student, Andy Le, analyzed the local microscopic response of the cells within the network. The project focuses on regular hexagonal networks designed at Centre de Biologie Structurale (CBS, France) and fabricated by Charlot's group (Institute of Electronics and Systems (IES), France). This falls under the umbrella of the third objective presented in Section 1.3. My contribution was presented along with Andy Le's results at the ICTAM2024 conference in Korea by Andy Vinh Le.

- *Le A.V. Bellenguez M. Darthenay-Kiennemann C. Bollaert C. Turcitu T. Charlot B. Pellicer A. Giansily Blaizot M. Virolle L. Fenech M. & Abkarian M. Blood rheology in the microcirculation, 26th International Congress of Theoretical and Applied Mechanics (ICTAM 2024).*

### 1.4.3 Collaborative Research on Retina Networks for Hydraulic Resistance Studies

The third project presents my contribution to a collaborative work with L. Julien (Sorbonne University), and Dr. Paques (15-20 Hopital National de la Vision, Paris, France). This project explores a 1D model of blood flow circulation of the retinal network to analyze the impact of pathologies on blood flow dynamics This project is separated into three main parts: theoretical and numerical model, experimental and clinical applications. The experimental objectives were to investigate the hydraulic resistance of the network with blood to compare with the theoretical model. The experiments offered new data on the distribution of RBC in a large network which enhances mathematical laws for modeling viscosity and red blood cell distribution. My specific contribution was on the experimental component where I conducted pressure-flow rate experiments to analyze the hydraulic resistance of the biomimetic retina on a chip perfused with different fluids viscosities (blood and glycerol) to determine the compliancy regime of the device. The project focuses on the biomimetic retina network designed and fabricated by Charlot's group (Institute of Electronics and Systems (IES), France). This falls under the umbrella of the third objective presented in Section 1.3. My contribution will be presented at the µTAS2024 conference along with Julien’s results.

- *Julien l. Le A.V. Turcitu T. Abkarian M. Coudène L. Paques M. José- Fullana J.M. Charlot B. Fenech M. Biomimetic Retina on a Chip for Characterization of Microvascular Dynamic The 28rd International Conference on Miniaturized Systems for Chemistry and Life Sciences (µTAS 2024), 2024.*

## 1.5 Organization and Structure of the Thesis

This thesis is structured into eight chapters. Chapter 1 introduces the research motivation, reviews pertinent literature, and outlines the research statement and objectives. It also provides an overview of the three experimental projects undertaken. Chapter 2 delves into the materials and methods of all three projects, describing the geometries of microfluidic devices, the microfabrication process, mechanical properties, blood preparation, and experimental setups. The three projects present the same methodology with slight variations that will be highlighted. Chapter 3 presents the results and discussion of the mechanical and hydraulic properties investigation of the tapered-parallel networks. Chapter 4 presents the results and the discussion of the hexagonal networks evaluation under variable red blood cell rigidity. Chapter 5 presents the results and discussion of the hydraulic resistance of the retina network under different fluid of varying viscosities. Chapter 6 discusses the devices uncertainties along with a comparison of the different pressure setups. Finally, Chapter 7 summarizes the findings and offers suggestions for future research.

# 2 Materials and methods

The ultimate goal of this research is to optimize microfluidic device design and contribute to hemorheology research. To achieve this goal, three main objectives were proposed that are addressed with three different projects. The objectives of this thesis are to investigate the mechanical properties of both PDMS and NOA devices, to obtain the compliance in the tapered-parallel networks fabricated with different materials and to investigate the pressure-flow rate relation of three different networks (tapered-parallel, hexagonal and retina). To achieve them, an experimental plan has been proposed with slight variations for each experimental project. This experimental plan includes the microfluidic devices geometries, the microfabrication, the mechanical properties, blood preparation and experimental setup.

## 2.1 Microfluidic Devices Geometries

This thesis contains three distinct projects that uses different microfluidic devices geometries. In the first project, three tapered-parallel channels with varying dimensions were employed to explore the hydraulic resistance and compliance of different materials. The second project utilized four hexagonal networks of varying lengths to examine the impact of red blood cell (RBC) rigidity on hydraulic resistance. In the third project, a retina network with diverse channel diameters and lengths was utilized to investigate the influence of varying fluid viscosities on hydraulic resistance.

### 2.1.1 Tapered-Parallel Network

The geometries of the microfluidic chips used were previously designed in Niko Lee-Yow's study and consists of two tapered chambers connected with parallel channels (Figure 9) [13]. The chip has an inlet path and two outlet paths. Three chips (A, B and C) of different dimensions were used. The dimensions of the parallel channels tapered chambers, and inlet and outlet paths for the different chips are presented in Table 2 and Table 3

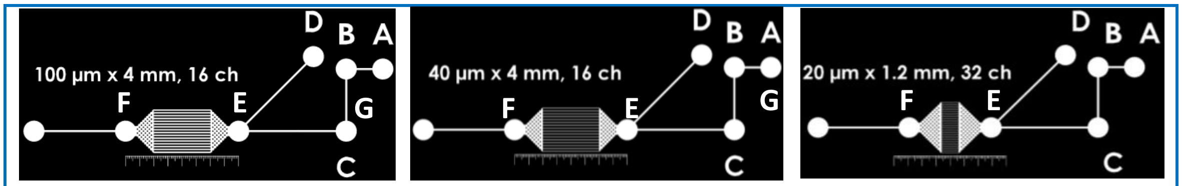

Chip A Chip B Chip C

**Figure 9: Mask used for SU-8 structures to make the PDMS stamp of a) chip A, b) chip B and c) chip C. The parallel channel widths are 100 µm for chip A, 40 µm for chip B and 20 µm for chip C.**

**Table 2: Parallel channels and tapered channels dimensions of different chips**

| **Parallel channels** | | | |
|---|---|---|---|
| **Parameters** | **A** | **B** | **C** |
| Smallest edge ($d_2$)(µm) | 100 | 40 | 20 |
| Longer edge ($d_1$)(µm) | 100 | 100 | 100 |
| Length (L) (µm) | 4000 | 4000 | 1200 |
| Number of parallel channels | 16 | 16 | 32 |
| **Tapered channels** | | | |
| Width of entrance ($b_1$)(µm) | 500 | 500 | 500 |
| Width of exit ($b_2$) (µm) | 3100 | 3100 | 3740 |
| Height of channel (h)(µm) | 100 | 100 | 100 |
| Radius of micropillar ($r_m$)(µm) | 50 | 50 | 50 |
| Length of tapered channels (λ)(µm) | 1270 | 1270 | 1591 |
| Half distance between fibers (Δ)(µm) | 50 | 50 | 50 |

**Table 3: Inlet and outlet channels dimensions**

| **Parameters** | **Inlet channel (Ports GF)** | **Outlet channel (Ports ED)** | **Outlet channel (Ports EC)** | **Outlet channel (Ports CB)** | **Outlet channel (Ports BA)** |
|---|---|---|---|---|---|
| Width ($w$)(µm) | 100 | 100 | 100 | 100 | 100 |
| Height ($h$)(µm) | 150 | 150 | 150 | 150 | 150 |
| Length (L) (µm) | 5000 | 6000 | 6129 | 2925 | 1104 |

### 2.1.2 Hexagonal Network

Four hexagonal networks were designed by Abkarian's group (CBS, France) and the molds were fabricated by Charlot's group (IES, France). The devices consist of an inlet channel, an outlet channel and a hexagonal grating. The inlet and outlet channels are 2 mm wide and approximately 100 µm in height as seen in Figure 10. The height of the hexagonal grating and the length of each individual channel are 5 µm. The microfluidic devices differentiate by the channel length ratio resulting in topological changes from a hexagon to a square-like design as seen in Figure 11. The length of the hexagonal networks and the channels length ratio are presented in Table 4. The chips were fabricated to have the same overall resistance.

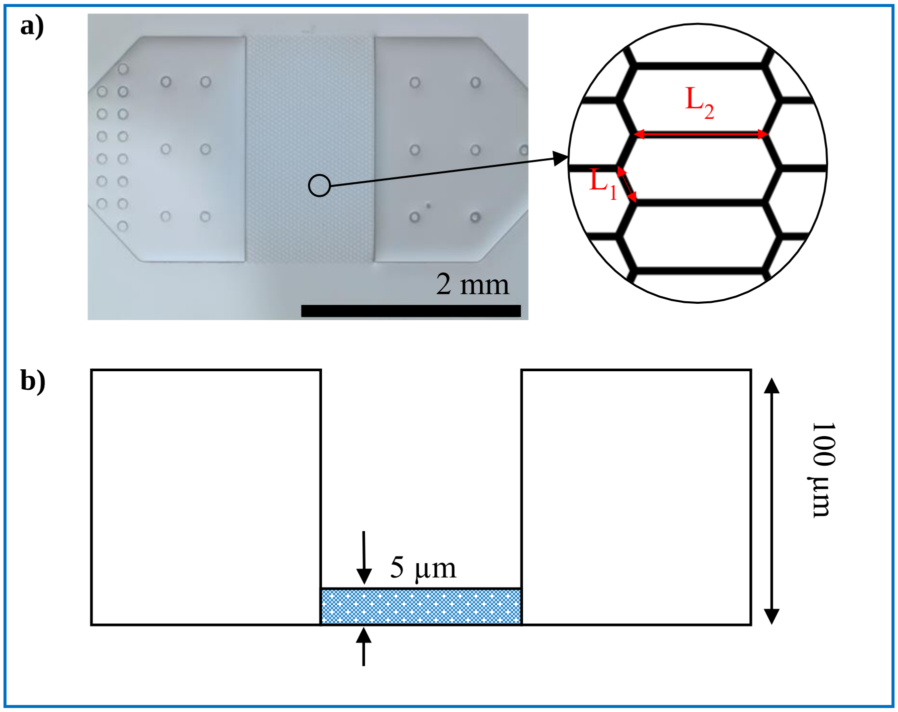

**Figure 10: a) Top view and b) side view of the PDMS hexagonal chip.**

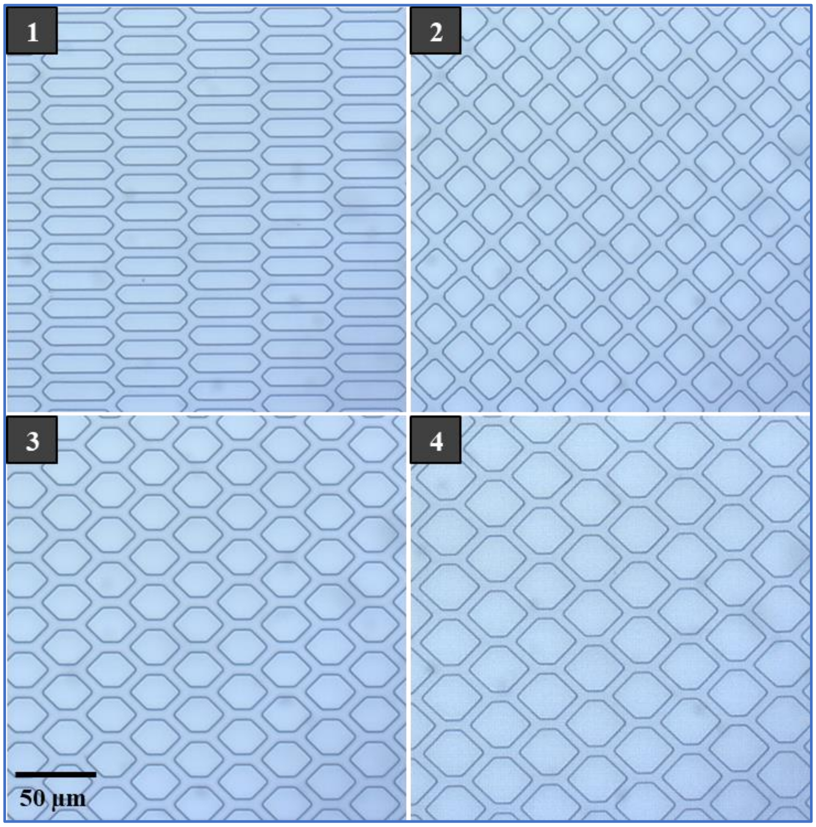

**Figure 11: Microscopic view of the different channel length of the hexagonal chips**

**Table 4: Length of the hexagonal networks and the channel length ratio**

| Chip | $L_1$(µm) | $L_2$(µm) | $L_2/L_1$ |
|---|---|---|---|
| 1 | 10 | 30 | 3 |
| 2 | 20 | 0 | 0 |
| 3 | 15 | 10 | 0.67 |
| 4 | 20 | 10 | 0.5 |

### 2.1.3 Retina Network

The retina network was designed by L. Julien, Sorbonne University, in collaboration with Dr. Paques (15-20 Hopital national de la vision, Paris, France). The molds were fabricated by Charlot's group (IES, France). The chip represents the arterial network of the retina, with blood arriving via the retinal artery (inlet) and the connection to the vascular network is represented by a constant vascular pressure at the output (in the crown) (Figure 12). The dimensions of the retina chip branches follow Murray's Law and a mother-daughter relation between the diameter of the channels as described in Julien thesis [62]. The diameters vary between 30-180 µm and the length of the channels vary between 40-100 µm. The overall dimension of the chip is 1 cm x 1 cm.

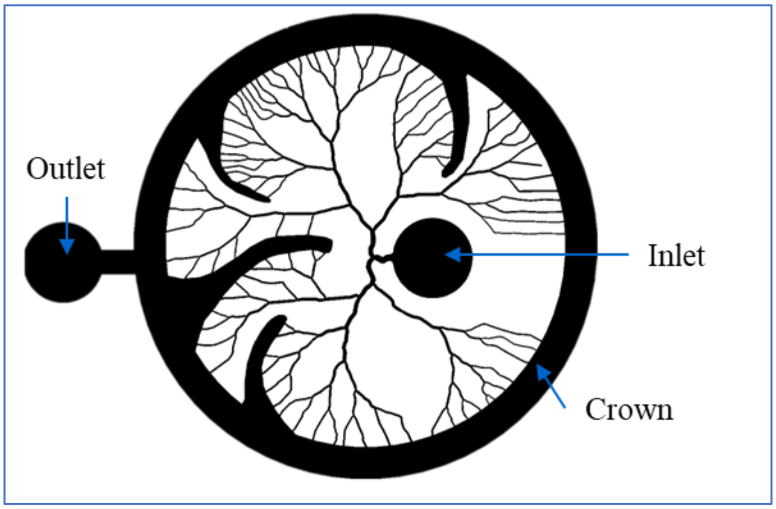

**Figure 12: Diagram of the retina chip design.**

## 2.2 Microfabrication

In this section, the microfabrication process for the different networks is presented. A SU-8 wafer has been used to fabricate the chips by conventional photolithography for the tapered-parallel networks and hexagonal networks, and by backside photolithography for the retina network. The NOA and PDMS fabrication process are also presented.

### 2.2.1 SU-8 Wafer Fabrication

### *2.2.1.1 Conventional Photolithography*

Conventional lithography was used to create tapered-parallel network (fabricated by Niko-Lee- Yow) and hexagonal networks (fabricated by Charlot's group, IES, France). The molds used for the replica molding of PDMS chips were made with SU-8 photoresist patterned on 3-inch silicon wafer. After Piranha solution cleaning (mixture of $H_2SO_4$ and $H_2O_2$) and nitrogen drying, a thin layer of SU-8 50 (MicroChem, Westborough, USA) was manually poured onto the surface of the silicon wafer and spin coated at 500 rpm with an acceleration of 100 rpm/s for 10 s [63]. Immediately after the spread step, a final speed of 1000 rpm was achieved at an acceleration of 300 rpm/s and held for a total of 30 s. After two-step soft baking at 65 °C for 10 min and 95 °C for 30 min, a thin layer of glycerol was used between the mask and wafer to improve the contact [63]. Glycerol was used to ensure a similar refractive index so the light will not refract in the gap between the wafer and mask [64]. The mask/glycerol/wafer was exposed to UV at 500–650 mJ/cm2 at 350–400 nm [63]. The mask used for the SU-8 structure imprint is negative, as shown in Figure 13. Post-exposure bakes at 65 °C for 1 min and at 95 °C for 10 min were completed on the SU-8 wafer [63]. Once the SU-8 wafer was cooled to room temperature, it was submerged into the SU-8 developer for 10 min, rinsed with isopropyl alcohol (99%) and dried with nitrogen gas.

#### *2.2.1.2 Backside Photolithography*

Backside lithography has been used for the retina’s wafers (fabricated by Charlot’s group, IES, France). Backside lithography differs from traditional photolithography by directing light through a lithography mask onto the backside of a transparent substrate rather than directly onto a resin-coated sample [65]. A mask is created on the samples surface through various techniques such as deposition engraving or lift-off microstructuring on a glass substrate. Exposing a uniform thickness of resin from the underside leads to comparable resolution to that of front-facing lithography when optimal exposure doses are applied [65]. SU-8 negative photoresist, commonly employed in microfluidics due to its high transparency in the 365 nm UV band, is used in this process [65]. A brief exposure just below the required doses is sufficient to solidify thick layers of SU-8 without necessitating perfect contact between the mask and the resin [65]. The inclusion of a diffuser is crucial for generating gradients in height relative to width. The diffuser disperses light from its surface based on its angular diffusion profile, akin to the distribution of material in plasma etching processes [65]. The efficacy of the diffuser, particularly its angular diffusion profile, is a critical determinant of the success of this technique [65].

### 2.2.2 NOA Fabrication

NOA63 was chosen due to its high viscosity (2500 cps) at 25 °C and low shrinkage of approximately 1.5% [10], [28], [66]. NOA devices are manufactured using a patterned PDMS stamp. The details of the NOA device manufacturing process are shown in Figure 13. Using a silanization process, the PDMS molded from the SU-8 wafer was used to fabricate the PDMS stamp. The PDMS-PDMS replica molding was adapted from Zhuang et al. [67]. The PDMS was created using a PDMS 5:1 mixture of main agent and curing agent, respectively. This creates a harder mold allowing the PDMS to act as a more effective mold during the silanization process [68], [69], [70]. The harder PDMS was placed in a vacuum chamber, directly above 2 drops of trichloro (1H 1H 2H 2H-perfluorooctyl) silane (PFOTS). The PDMS master was de-gassed for 15–20 min causing the PFOTS to create a thin layer over the PDMS surface. The PDMS was then placed on a hot plate for 10 min at 150 °C. It could then be used as a mold for the PDMS stamp by using a traditional 10:1 ratio of main agent to curing agent, as typically used in microfluidic devices [70]. The 10:1 ratio was then poured on top of the PDMS and heated at 75°C in the oven for 1 h. The PDMS stamp was finally cut away from the PDMS.

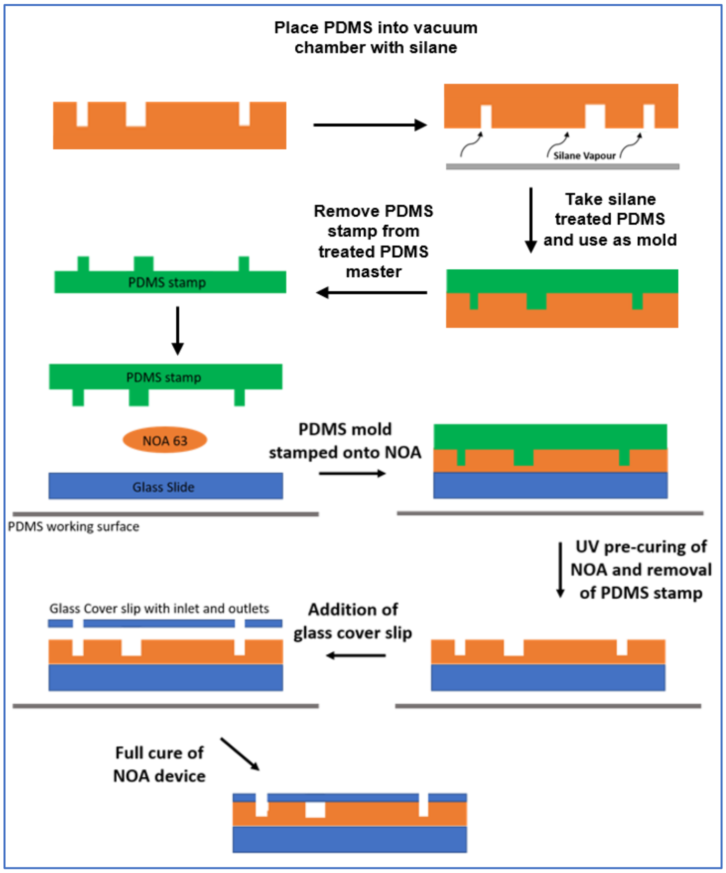

**Figure 13: Schematic layout of the NOA device manufacturing method using NOA 63.**

The manufacturing method of the NOA63 microfluidic devices was adapted from the technique presented by Sim, Jae Hwan et al. [66]. A 1.25 cm diameter circle of NOA63 was dispensed onto a standard glass slide. The PDMS stamp generated from the double molding with a classical SU-8 wafer was used to manually stamp the uncured NOA63. The stamped NOA63 was then placed under 365 nm wavelength UV light of intensity 40.25 mW/cm$^2$, for 10 s causing the glue to stay in a precured state for a total energy exposure of 402.5 mJ/cm$^2$. Therefore, the stamped channels were retained by the NOA. The PDMS stamp was removed from the NOA, and a glass cover slip was placed, and aligned, on top of the precured NOA. The cover slip was prepared in advance with laser cut holes for the appropriate inlet and outlet ports using a CO$^2$ laser etching machine (Epilog Laser). The etching machine was set to a speed of 85% and a power of

90%. The coverslip was secured to a wooden surface and 10 laser shots were used to create the inlet and outlet holes. Once aligned atop the precured NOA63, the entire NOA63 device was placed under UV light at an intensity of 40.25 mW/cm$^2$ and a wavelength of 365 nm for 20 min for a total energy exposure of 241.5 J/cm$^2$. An airtight adhesive bond formed between the glass and the precured NOA. PDMS pieces were pre-punched at a 20-gauge diameter and plasma-bonded onto the glass coverslip, completing the NOA device.

### 2.2.3 PDMS Fabrication

The PDMS devices were manufactured using the SU-8 wafer with a patterned mask. The manufacturing process for the PDMS microfluidic devices is detailed in Figure 14.

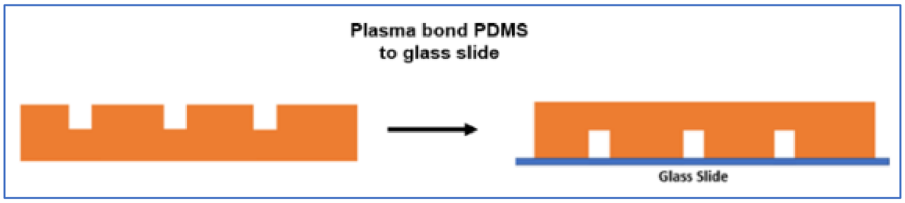

**Figure 14: Schematic layout of the PDMS device manufacturing method using a PDMS device. The PDMS device is taken from the patterned wafer and plasma bonded to a glass cover slip.**

The PDMS was made by using a traditional 10:1 ratio of main agent to curing agent, typically used in microfluidic devices [70]. This mixture was de-gassed for 1 h until no air bubbles were present. The 10:1 ratio was then poured on top of the SU-8 wafer and heated at 75 °C in the oven for 1 h. The PDMS device was finally cut away from the SU-8 wafer. Inlet and outlet holes were pre-punched at a 20-gauge diameter into the device, and it was plasma-bonded to a glass slide.

## 2.3 Mechanical Properties

The mechanical properties of PDMS and NOA were investigated to achieve the first objective. This includes characterizing surface roughness, tensile strength, channel width deformation, and contact angle. Glycerol viscosity was also investigated for the third project to observe the effect of viscosity on the retina network.

### 2.3.1 Surface Roughness

The surface roughness was measured using the *DektakXT* profilometer (Bruker Corporation, Billerica, MA, USA). A PDMS sample of 34 mm length, width of 14 mm and thickness of 2 mm was used. A sample of NOA 63 of 30 mm length, 14 mm width and thickness of 2 mm was used. The PDMS samples were made on a clean SU-8 wafer to assure the surface did not have imperfections. The NOA sample was made on the PDMS surface in contact with the wafer. Three tests were per-formed for each sample. For the NOA, the tests were performed on a length of 20 mm with leveling. The PDMS tests were performed on a length of 25 mm with no leveling.

### 2.3.2 Tensile Strength Test

The tensile strengths of the PDMS and NOA63 was measured using the *Instron 4482* materials testing machine (Instron Corporation, Norwood, MA, USA). Three PDMS samples measuring 74 mm in length, 26 mm in width and 3 mm in height were tested with tensile grips of 10 N. Similarly, three NOA63 samples of 65 mm length, 20 mm in width and 1.6 mm in height were tested using tensile grips of 10 kN. All samples were tested at a rate of 15 mm/min until failure.

### 2.3.3 Channels Width Deformation

The channels’ deformation under flow rate conditions was measured to better understand the compliance in the chips. For this purpose, images of the channels were captured using a microscope featuring 40× objective while maintaining a constant flow rate. Deionized water was pushed from a 500 µL Hamilton syringe by a syringe pump at rates of 25, 50 and 100 µL/h. The channel width was then measured for each flow rate using ImageJ 1.53.

### 2.3.4 Contact Angle

The contact angle measurement was used to observe the hydrophilic and hydrophobic properties of the materials. The same samples of PDMS and NOA63 were used for surface roughness measurements. Both PDMS and NOA samples were cleaned with tape to remove any particles. Three tests were performed on each sample with and without plasma treatment. The tests of the samples without the plasma treatment were first performed followed by the tests with plasma treatment. A plastic syringe was utilized to distribute 1 microliter of water on each sample. A digital microscope captured side-view images, and each sample underwent three tests. The contact angle was then measured using ImageJ ROI manager. The plasma treatment was made using the Laboratory Corona Treater (Electro-Technic Products inc., Chicago, IL, USA) device for about 1 min on each sample. This device distributes the plasma using an electric current. Plasma was applied to the surface of the material, causing the chips to become hydrophilic.

### 2.3.5 Glycerol Viscosity

The *m-VROC* viscosimeter (RheoSense, San Ramon, CA, USA) was used to measure the viscosity of three different concentrations of glycerol. Glycerol was used due to its viscous nature and Newtonian behaviour. The concentrations of glycerol were made by mixing deionized water with glycerol at 40%, 60% and 80% of glycerol. The viscosity was measured three times for all concentrations.

## 2.4 Blood Preparation

Blood samples were obtained from the laboratory of hematology at Centre Hospitalier Universitaire, Hopital Saint-Eloi in Montpellier France and from volunteers in Ottawa, Canada with approval of the ethics committee at the University of Ottawa (ETHICS CODE H03-19-3441). To extract the RBC from the blood the following method was used. The blood sample was first filtered with a white blood cell (WBC) filter to remove the WBC to get cleaner images of the RBC in the network. Then, the blood sample was centrifuged once for 5 min at 400 g. The plasma sitting at the top of the sample was removed. PBS mixed with glucose was added to the RBC and centrifuged for 5 min at 400 g. After the centrifugation, the PBS and glucose solution was removed, more solution was added to the RBC, and it was centrifuged again for 5 min at 400 g. This step was repeated three more times for a total of five centrifugations.

### 2.4.1 Sample Preparation

#### *2.4.1.1 RBC*

Once the blood was cleaned a control solution was prepared at 10% or 20% hematocrit. To do so, 50 µl of RBC were mixed with 450 µl of OptiPrep and PBS mixture and 100 µl of RBC were mixed with 400 µl of OptiPrep and PBS mixture to get 10% HCT and 20% HCT respectively. OptiPrep acts as a density gradient medium, preventing red blood cells from settling at the bottom of the tube while also homogenizing their distribution throughout the tubing.

#### *2.4.1.2 RBC with Diamide*

To investigate the influence of RBC's deformation properties on the hexagonal networks, the RBCs were rigidified using diamide. Diamide increases membrane rigidity by increasing protein to protein associations with induced formation of inter- and intra- disulfide bonds [55]. Two different concentrations of diamide in a PBS and glucose solution were made to see the effect of diamide on RBC membrane. The chosen concentrations are 50 µM and 200 µM. These concentrations were chosen due to low sphericity of RBC and low relative rigidity of RBC when compared with untreated RBC [55]. Then, 50 µl of RBC were mixed with 450 µl of the different diamide concentrations and put on a test tube heater for 1hr at 37°C. Subsequently, it was centrifuged at 400 g for 5 min. The excess diamide was removed and replaced by OptiPrep, PBS and glucose solution.

### 2.4.2 Circularity of Red Blood Cells

The circularity of RBC untreated and treated with diamide was measured to investigate the effect of RBC rigidity in hexagonal networks. Circularity is the measurement of how round an object is. It is the ratio of the actual perimeter of a particle to the perimeter of a circle of the same area [71], [72]. A value of 1 signifies the cell is a perfect circle and that the cell is swelling and a value lesser than 1 signifies an irregular shape. The circularity is calculated using the following equation:

$$\text{Circularity} = \frac{\sqrt{4\pi A}}{\text{P}} \qquad \text{Equation 7 [71]}$$

where $A$ is the area of the cell and P the perimeter of the cell.

The circularity of RBCs was measured using Fiji by ImageJ. The initial images were adjusted with the brightness/contrast, window/level and the threshold. Dilate, Erode and Fill holes functions under the binary process were used to remove unwanted points and to fill the area of the RBCs. The area and perimeter were set for measurement. Using Analyze particles, the area and perimeter of the RBCs were measured. 10 RBC shapes from the different images were chosen and their circularity was averaged.

### 2.4.3 Deformation of RBC Using Ektacytometry

Ektacytometry, utilizing the *RheoScan-AnD 300* device by RheoMeditech (Seoul, South Korea), was employed to assess the deformability of red blood cells (RBCs). A suspension of RBCs was prepared by combining 6 µl of blood with 0.5 ml of polyvinylpyrrolidone (PVP) dissolved in a PBS solution, with an osmolarity of 300 mOsm/kg and a viscosity of 30 cP. This RBC suspension was then introduced into a microfluidic chip. Within this setup, the RBCs underwent deformation induced by a pump applying shear stress, while being illuminated by a laser beam. A diffraction pattern generated on a computer screen enabled the measurement of shear stress and elongation index. This procedure was iterated across varying concentrations of blood treated with diamide for comprehensive analysis.

The Lineweaver-Burk plot was used to fit the data of the elongation index over the shear stress. This model takes the inverse of the elongation index (1/EI) (y-axis) and the inverse of the shear stress (1/SS) (x-axis) [73]. These values will form a linear curve where the slope ($a$) and the intercept ($b$) can be extracted. The inverse of the intercept is the maximal EI ($EI_{max}$) and the slope multiplied by $EI_{max}$ is the half shear stress (½ SS) [73]. To fit the data, this equation is used:

$$\text{Lineweaver} - \text{Burk} = \frac{SS * EI_{max}}{SS + a/b} \qquad \text{Equation 8}$$

## 2.5 Experimental Setup

To optimize microfluidic devices, pressure-controlled setups, and a syringe pump setup can be used. In this section, two pressure controlled setups have been used to estimate the hydraulic resistance in the devices (tapered-parallel, hexagonal and retina network). These setups will be presented along with the analysis. Then, a syringe pump setup that allows the estimation of the compliance in the tapered-parallel network will be presented along with the analysis.

### 2.5.1 Pressure Controlled Setup for the Resistance of Microfluidic Devices.

Pressure driven setups are essential for creating physiologically relevant conditions in applications that aim to mimic biological systems, such as organs-on-chips or microvascular networks. Two different pressure-controlled setups have been proposed in this research to optimize microfluidic design and contribute to hemorheology research. A single pressure-controlled setup was used to investigate the hydraulic resistance in the tapered-parallel network and to observe the effect of viscosity on the hydraulic resistance of the retina network, while the dual pressure-controlled setup was used to investigate the effect of RBC rigidity on the hydraulic resistance of the hexagonal network.

#### *2.5.1.1 Single Pressure Controller Setup*

Resistance can be defined as the slope of the linear relationship between pressure and flow rate. A pressure-controlled system (Flow EZ, Fluigent, France) coupled with a microflow sensor (Flow Unit S, Fluigent, France) was used to test the resistance for the tapered-parallel network and the retina network. The fluidic circuit consisted of rigid components with low compliant properties, which included a 20-gauge metal tubes and small but rigid polymer tubing. Additionally, a 0.2 µm filter was placed at the top of the reservoir to filter the deionized water to prevent the flow meter from clogging for the tapered-parallel networks. The filter was not used for the retina network where blood and glycerol concentrations were used. A detailed flow chart of the experimental setup can be seen in Figure 15. Pressure was reduced by 0.5 mbar every 20 s from around 100 µL/h until no flow rate was detected. Pressure-flow rate data were collected with and without the chip and analyzed to calculate the resistance. The process was repeated three times for all chips for both materials. The average flow rate for each applied pressure was used to plot the pressure-flow relation. The chip's resistance was then calculated by deducting the resistance of the tubing and filter alone from the resistance of the whole circuit, which included the chip.

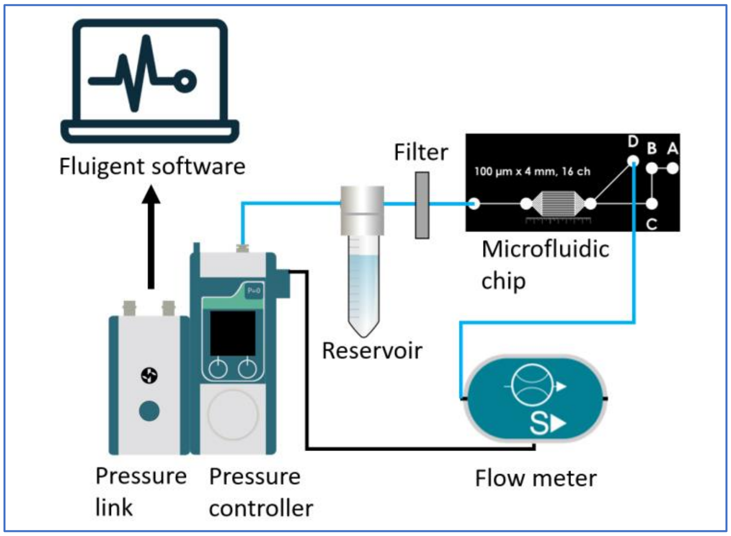

**Figure 15: Pressure control setup for the resistance testing of the tapered-parallel network and retina.**

#### *2.5.1.2 Dual Pressure Controller Setup*

This setup measures the variation of pressure and the flow rate. A two-pressure controller setup was proposed to provide a known variation of pressure for the hexagonal networks. This setup is composed of two pressure-controlled systems (Flow EZ, Fluigent, France) coupled with a microflow sensor (Flow Unit S, Fluigent, France) and a high-speed camera (NOVA R5-4k, Photron, Japan) as shown in Figure 16. The fluidic circuit consisted of rigid components with low compliant properties, which include 20-gauge metal tubes and small but rigid polymer tubing. The pressure controller 1 flows OptiPrep-PBS-Glucose solution into the flow meter to the exit of the microfluidic device and the pressure controller 2 flows blood in the microfluidic chip. The setup is first used to determine the pressure-flow rate data for the calibration solution (OptiPrep-PBS-Glucose solution). To do so, the pressure controller 1 first decreases the pressure by 50 mbar from

810 mbar to 60 mbar and then it increases the pressure back to 810 mbar while the pressure controller 2 remains at 10 mbar. Then, to observe the RBC passage in the microfluidic device, the pressure controller 2 first decreases the pressure by 50 mbar from 810 mbar to 60 mbar and then it increases the pressure back to 810 mbar while the pressure controller 1 remains at a constant pressure of 10 mbar throughout the rest of the experiment. This process is repeated two times for each chip to take images of a wider view and a focalized view of the hexagonal networks with the high-speed camera connected to a microscope. For the wider view, images are taken at every pressure at 1000 frame rate per second (fps) with a 10x objective. For the focalized view, images are taken at every pressure at frame rates per second of 4000, 2000 and 1244 with a 40x objective for pressure between 510-810 mbar, 210-510 mbar and 60-210 mbar respectively.

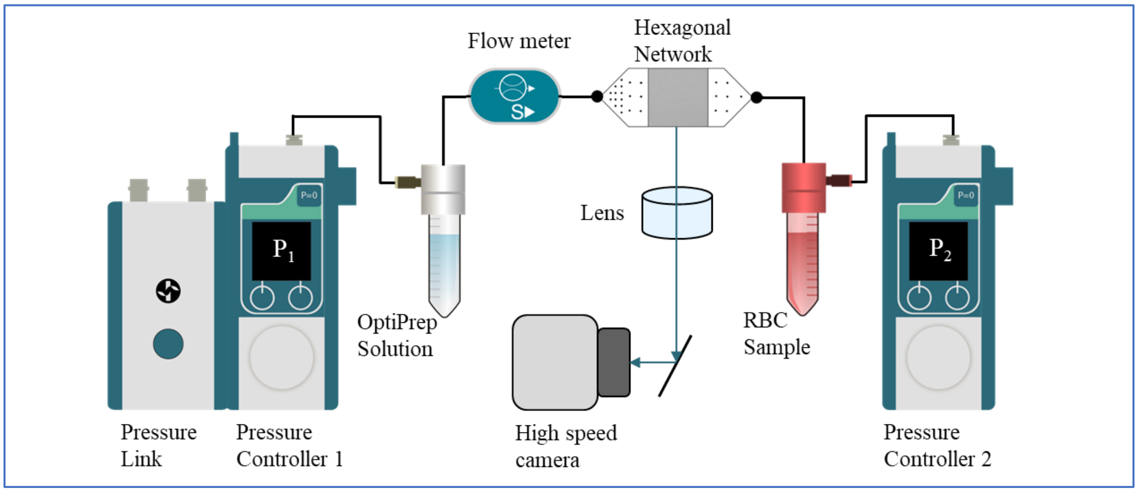

**Figure 16: Two pressure controllers' setup for the resistance testing of the hexagonal networks.**

### 2.5.2 Experimental and Theoretical Hydraulic Resistance Analysis

In this section, the theoretical and experimental resistance of the microfluidic devices will be presented. The three projects followed the same analysis. The analysis for the theoretical and experimental hydraulic resistance estimation is presented in this section. The three projects followed the same analysis.

#### *2.5.2.1 Experimental Hydraulic Resistance Estimation*

For the three projects, the same analysis was performed. The experimental resistance of the chip can be obtained by plotting the pressure over the mean flow rate from the data recorded with the pressure-controlled setups. The regression line is then modeled as follows:

$$\Delta \mathrm{P} = \mathrm{R_{exp}} \times Q + p_0 \qquad \text{Equation 9}$$

where $\mathrm{R_{exp}}$, the slope, is the experimental resistance of the microfluidic device, $Q$ is the average flow rate at each pressure and $p_0$ is the initial pressure. To get the experimental resistance of only the chip, the slope of the regression line with the chip (chip plus tubes) and without the chip (only tubes) must be modeled. Then, the slope of the system without the chip can be subtracted from the slope of the full system (with the chip) as follows:

$$\mathrm{R_{chip_{exp}}} = \mathrm{R}_{full\ system} - R_{no\ chip} \qquad \text{Equation 10}$$

When the hydraulic resistance of the tubings ($R_{no\ chip}$) is at least 100 times smaller than the hydraulic resistance of the full system ($\mathrm{R}_{full\ system}$), the resistance of the tubings was considered negligeable since it has low to no impact on the hydraulic resistance of the chip.

#### *2.5.2.2 Theoretical Hydraulic Resistance*

The theoretical resistance of each device is determined by calculating the hydraulic resistance of each channel, whether arranged in parallel or series, using the appropriate hydraulic resistance equations for rectangular, circular, and tapered channels as seen in Table 1 (Chapter 1).

### 2.5.3 Syringe Pump Setup for the Characteristic Time of the Microfluidic Devices

A flow-control system was used to measure the characteristic time of the tapered-parallel network to investigate the compliance in microfluidics devices fabricated with PDMS and NOA. The characteristic time was measured by analyzing the time delay of the output flow rate versus the flow rate imposed by a pump. The setup consisted of a glass syringe (500 µL Hamilton) mounted on a syringe pump (Nexus 3000, Chemyx, Stafford, TX, USA) coupled with a flowmeter (Flow unit S, Fluigent, France). The fluidic circuit was composed of 20-gauge metal tubes, and small but rigid polymer tubing. As for the pressure control setup, a filter was placed at the tip of the syringe to filter the deionized water. A detailed flow chart of the experimental setup can be seen in Figure 17. The syringe pump was set to accommodate flow rates of 25 µL/h, 50 µL/h, and 100 µL/h through the microfluidic device. The process was repeated 3 times and the average results at each point were used to plot the flow over time for each chip and flow rate. NOA and PDMS devices were tested.

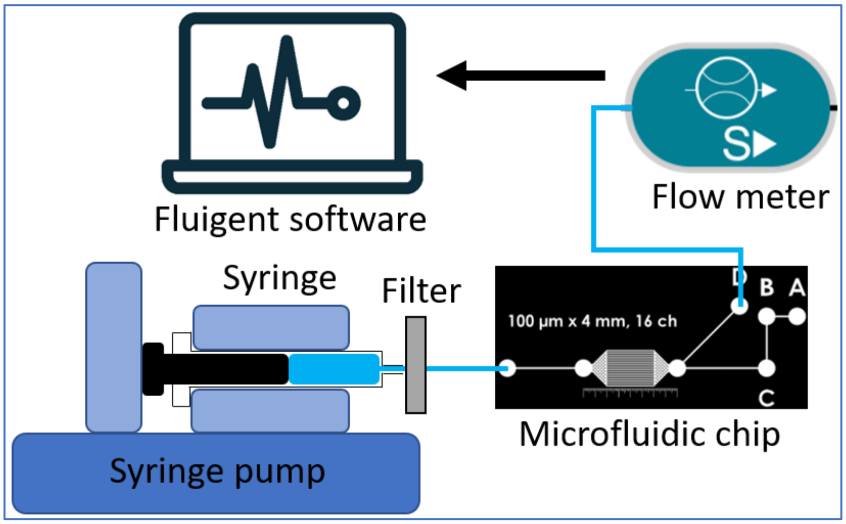

**Figure 17: Syringe pump setup for the characteristic time testing of microfluidic devices.**

### *2.5.3.1 Two-Element Resistance Compliance (RC) Hydraulic Circuit Model*

The flow of the system can be described by:

$$Q_{in} - Q_{out} = Q_c \qquad \text{Equation 11}$$

where $Q_{in}$ is the inflow rate to the system, controlled by the syringe pump. $Q_{out}$ is the outflow rate of the system measured by the flow meter, and $Q_c$ is the rate of storage of the system itself. $Q_c$ can be further described by:

$$Q_c = C\frac{dP}{dt} \qquad \text{Equation 12}$$

where $C$ is the compliance of the system and $\frac{dP}{dt}$ is the pressure change over time inside the system. This means the volumetric rate of storage of the system is directly related to the compliance of the system. $Q_{out}$ can be defined, assuming Hagen–Poiseuille flow, as:

$$Q_{out} = \frac{\Delta P}{R_s} \qquad \text{Equation 13}$$

where $\Delta P$ is the drop-in pressure of the system, and $R_s$ is the peripheral resistance. When the pressure at the outflow rate is assumed to be close to zero, it is reduced to the pressure within the storage chamber. Hence, Equation 11-Equation 13 can be re-written as:

$$Q_{in} - \frac{p}{R_s} = C\frac{dp}{dt} \qquad \text{Equation 14}$$

Integrating to solve for $p(t)$ using initial conditions of $p = p_o$ (initial pressure) and $t = 0$ (time), the pressure can be written as:

$$p(t) = R_s Q_{in} - (R_s Q_{in} - p_0)e^{-\left(\frac{t}{R_s C}\right)} \qquad \text{Equation 15}$$

where $p_0$ is the initial pressure and $t$ is the time. From Equation 14, $dp/dt$ can be rewritten as:

$$\frac{dp}{dt} = \left(\frac{R_s Q_{in} - p_0}{R_s C}\right)e^{-\left(\frac{t}{R_s C}\right)} \qquad \text{Equation 16}$$

Combining Equation 16, Equation 14, Equation 12 and Equation 11, the system equation can be rewritten as:

$$Q_{out} = Q_{in} - \left(\frac{R_s Q_{in} - p_0}{R_s}\right) e^{\left(-\frac{t}{R_s C}\right)} \qquad \text{Equation 17}$$

where $p_o$ is the initial pressure of the system, t is the time, and $R_sC$ represents the characteristic time of the system.

#### 2.5.3.2 Characteristic Time and Compliance

The characteristic time of each trial is calculated and used to compare the compliance of the system. This is assuming that the resistance of the external system is constant and the only change in compliance from the system comes from the microfluidic device.

The outflow rate of the system, $Q_{out}$ (which is a function of time $t$), can then be modeled using the following equation:

$$Q_{out} = A - Be^{-(\frac{t}{D})} \qquad \text{Equation 18}$$

The three constants are used to fit the raw data, acquired experimentally, from Equation 17. The constant $A$ represents the $Q_{in}$, the constant $B$ represents the maximum rate of storage, and the constant $D$ is the characteristic time of the system.

With the characteristic time, the compliance can be calculated using the following equation:

$$C = \frac{\tau}{R_{chip_{exp}}} \qquad \text{Equation 19}$$

where $C$ is compliance, $\tau$ is the characteristic time experimentally found for PDMS or NOA using Equation 11-Equation 18, and $R_{chip_{exp}}$ is the total experimental resistance of the microfluidic device found using the pressure controller.

### 2.5.4 Statistical Analysis

Unpaired Student’s t test was used for comparisons between the tapered-parallel networks fabricated with NOA and PDMS. GraphPad Prism 9 was used to perform the statistical tests and the graphical representations. A p-value less than 0.05 was considered statistically significant. The data were considered a normal distribution, due to the nature of the data describing a physical property of a material [74].

# 3 Investigation of Mechanical and Hydraulic Properties of Tapered-Parallel Networks: Results and Discussion

This chapter investigates the mechanical and hydraulic properties of the tapered-parallel networks. First, the mechanical properties, including surface roughness, tensile strength, contact angle, and channel deformation of PDMS and NOA were thoroughly examined to understand the performance characteristics of each material. Then, the hydraulic resistance was measured using water as the testing fluid. Finally, the compliance of these devices is quantified under flow conditions. The results aim to provide insights into the optimal material selection and network design for enhancing the performance and reliability of microfluidic devices.

## 3.1 Results

### 3.1.1 Mechanical Properties

#### *3.1.1.1 Surface Roughness and Tensile Strength*

The surface roughness of NOA63 and PDMS was found in terms of the arithmetic mean height of primary profile (Pa) and the root mean square height of the primary profile (Pq). The results are presented in Table 5. The samples of NOA63 and PDMS underwent three tensile strength tests each with the Instron machine. The average Young's modulus found for each material is compared to the theoretical values in Table 5.

**Table 5: Arithmetic mean height of the primary profile (Pa) and root mean square height of the primary profile (Pq) of the surface samples and experimental Young's modulus of NOA63 and PDMS, as well as those found in the literature.**

| Sample | Pa (µm) | Pq (µm) | Experimental Young's Modulus (MPa) | Literature Young's Modulus (MPa) |
|---|---|---|---|---|
| **NOA63** | 1600 ± 80 | 1900 ± 100 | 1700 ± 200 | 1655 [75] |
| **PDMS** | 150 ± 4 | 170 ± 4 | 2 ± 0.2 | 1-3 [15], [25], [26] |

It was observed that NOA63 has an arithmetic mean height of the primary profile and root mean square height about 10.6 times higher and 11.0 times higher than the PDMS, respectively.

### *3.1.1.2 Channels Width Deformation*

The tapered-parallel channels deformation of NOA63 and PDMS microfluidic devices were measured using microscopy and ImageJ at the different flow rates (25, 50 and 100 µL/h). The average values of these measurements are presented in Figure 18.

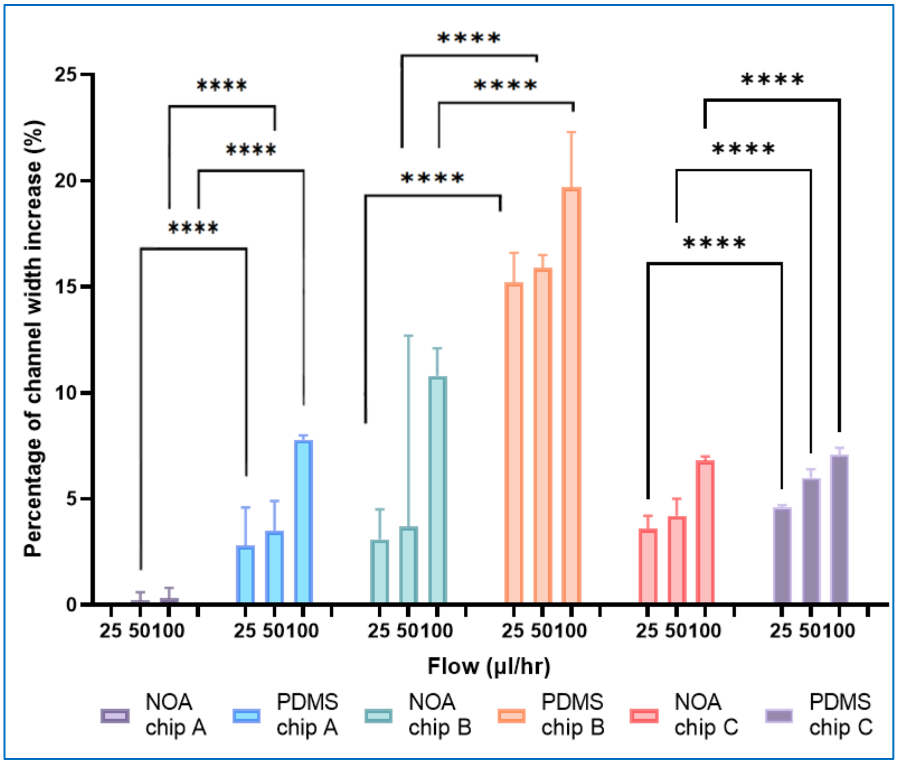

**Figure 18: Comparison of NOA and PDMS channels' width deformation of chip A, B and C at the different flow rates (25, 50 and at 100 µL/h). The initial channel width of the PDMS chip A is 95.4 ± 3.00 µm, that of chip B is 36 ± 2.30 µm and that of chip C is 17.7 ± 1.10 µm. The initial channel width of NOA chip A is 101.7 ± 8.00 µm, chip B is 38.2 ± 1.90 µm and chip C is 25.6± 1.10 µm. (**** *p*-value < 0.0001).**

It was observed that all PDMS devices have a lower initial channel width than NOA devices: 95.4 ± 3.00 µm vs. 101.7 ± 8.00 µm, 36.0 ± 2.30 µm vs. 38.2 ± 1.90 µm and 17.7 ± 1.10 µm vs. 25.6 ± 1.10 µm for PDMS vs. NOA in chip A, B and C, respectively. For all three chips, an increase in the channel width can be observed for the PDMS device as the flow rate increases. For the NOA devices, chip B and C show an increase in the channel width as the flow rate increases, but chip A displays a constant channel width. For chip A, at 100 µL/h, there is an increase of 7.8% for the PDMS device and of 0.2% for the NOA device. For chip B, at 100 µL/h, there is an increase of 19.7% for the PDMS and of 10.8% for the NOA device. Chip B has the highest increase in the percentage of channel width. For chip C, at 100 µL/h, there is an increase of 7.1% for the PDMS device and of 6.8% for the NOA device. PDMS shows a higher channel increase as the flow rate increases for chip A, B and C than NOA.

#### *3.1.1.3 Contact angle*

The contact angle of the NOA63 and PDMS samples was obtained with and without portable plasma treatment. Figure 19 illustrates the contact angle of a water droplet on the surfaces.

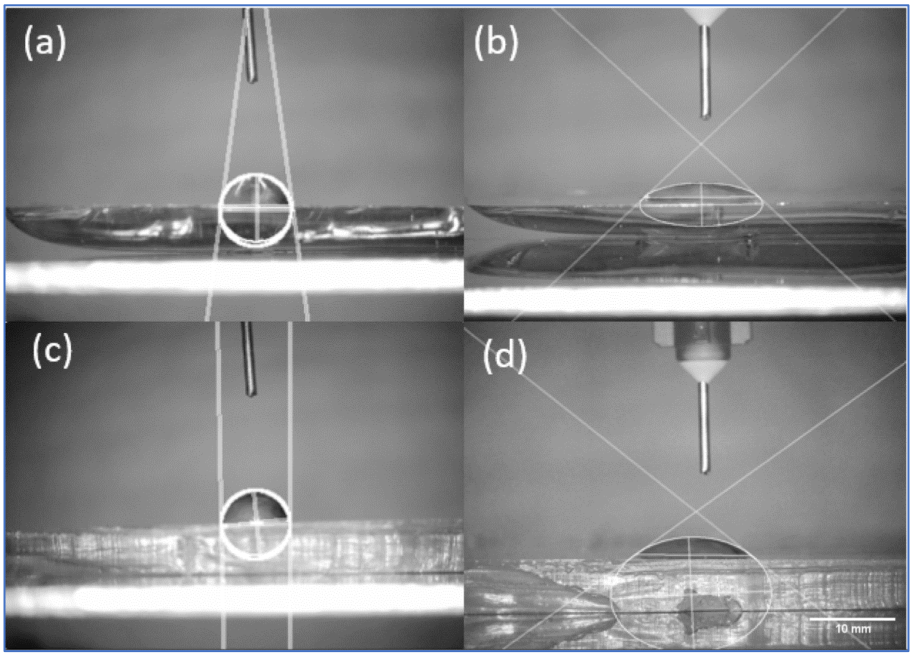

**Figure 19: Contact angle for (a) NOA63 without plasma treatment (81.4° ± 4.9), (b) NOA63 with plasma treatment (44.9° ± 3.1), (c) PDMS without plasma treatment (91.4° ± 1.9) and (d) PDMS with plasma treatment (32.1° ± 4.4).**

The results for the contact angle without and with plasma treatment for NOA and PDMS are, respectively, 81.4° ± 4.9, 44.9° ± 3.1, 91.4° ± 1.9 and 32.1° ± 4.4. A higher contact angle means the surface is more hydrophobic, while a lower contact angle means a more hydrophilic surface. By treating the materials with the plasma device, it can be observed that the contact angle decreases for both materials. This means that microfluidic devices become more hydrophilic after plasma treatment. Without plasma treatment, PDMS is more hydrophobic than NOA, and with plasma treatment, NOA is more hydrophobic than PDMS.

### 3.1.2 Resistance Estimation

The hydraulic resistances of the chips were found by following the procedure for a single pressure-controlled setup (Section 2.5.1.1) and analyzed using the experimental hydraulic resistance estimation procedure described in Section 2.5.2.1. Examples of the pressure as a function of the flow rate are presented in Figure 20 and the hydraulic resistances are presented in Table 6.

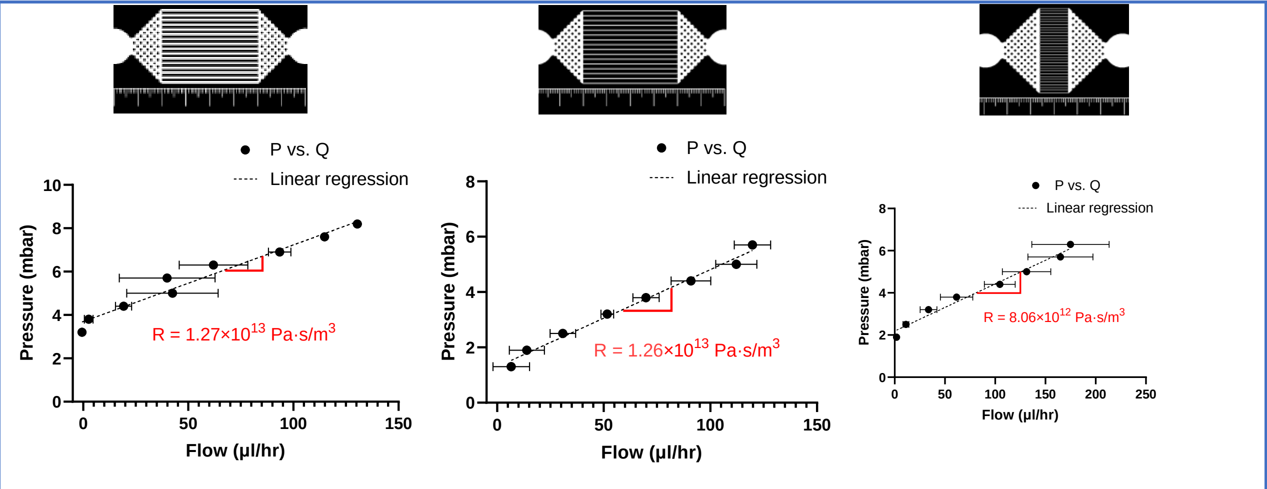

(a) (b) (c)

**Figure 20: Examples of the pressure as a function of the flow rate for the full hydrodynamic system of (a) NOA63 chip A, (b) PDMS chip A and (c) without the chip.**

By subtracting the experimental resistance without a chip from the experimental resistance of the NOA63 or PDMS, the experimental resistance of the chip can be found. The experimental resistances of the microfluidic devices are compared to the theoretical values in Table 6. The theoretical resistance of each device is determined by calculating the hydraulic resistance of each channel, whether arranged in parallel or series, using the appropriate hydraulic resistance equations for rectangular, circular, and tapered channels as seen in Table 1 (Chapter 1).

**Table 6: Experimental resistance of all 3 chips of NOA63 and PDMS and the theoretical resistance. The theoretical resistance range is calculated with the initial channel width dimension and the larger width with deformation.**

| Chip | Theoretical Resistance ($10^{12}$ Pa·s/m$^3$) | NOA63 Experimental Resistance ($10^{12}$ Pa·s/m$^3$) | PDMS Experimental Resistance ($10^{12}$ Pa·s/m$^3$) |
|---|---|---|---|
| **A** | 4.78–4.79 | 4.64 | 4.54 |
| **B** | 5.34–5.66 | 5.44 | 5.65 |
| **C** | 5.09–5.75 | 5.44 | 5.04 |

### 3.1.3 Characteristic Time Estimation

Examples of the flow rate as a function of the time for both NOA and PDMS chip A are presented in Figure 21.

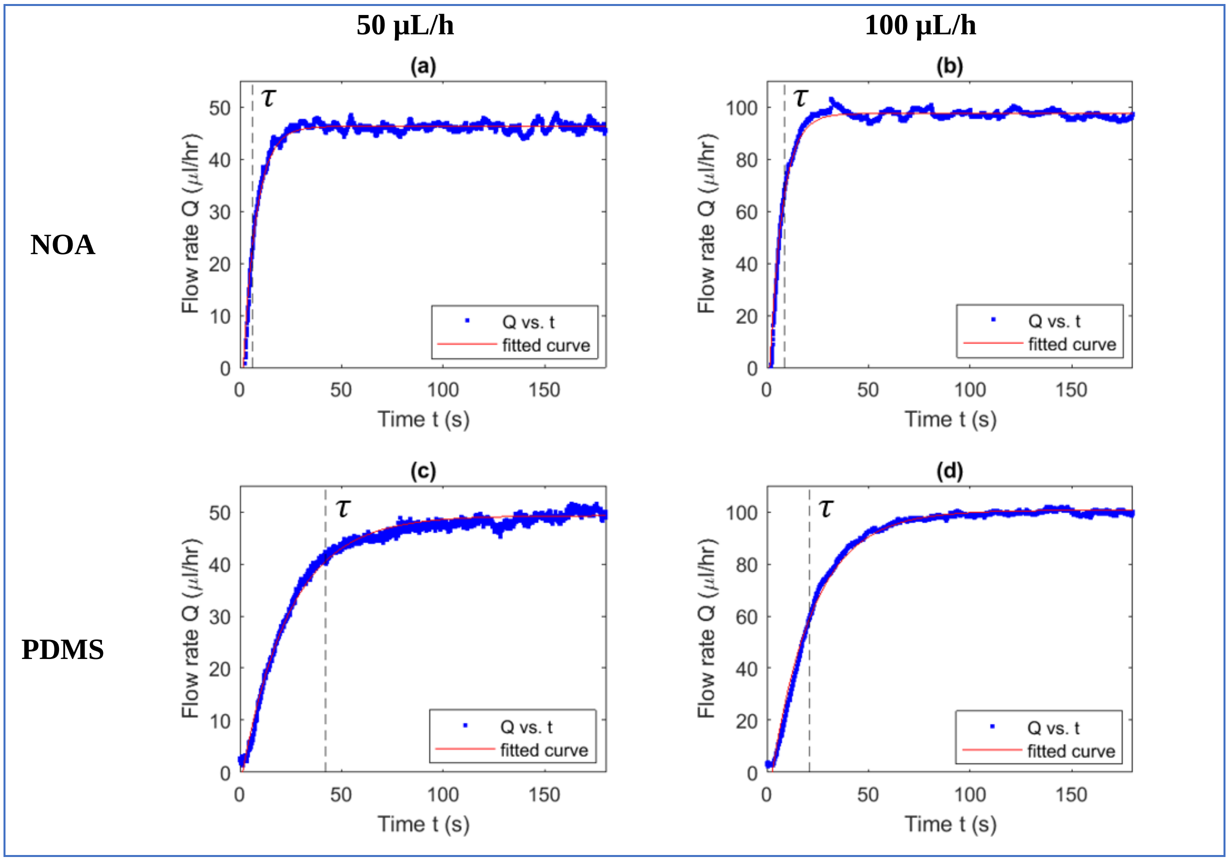

**Figure 21: Examples of flow rate versus time graphs for chip A (a) at flow rate of 50 µL/h for NOA63, (b) at flow rate of 100 µL/h for NOA 63, (c) at flow rate of 50 µL/h for PDMS, and (d) at flow rate of 100 µL/h for PDMS. Each device shows a significant initial rise from zero to the plateau value (Qout) measured from the Fluigent Flow Meter (S).**

All the PDMS and NOA63 trials' characteristic times were averaged and are graphed in Figure 22.

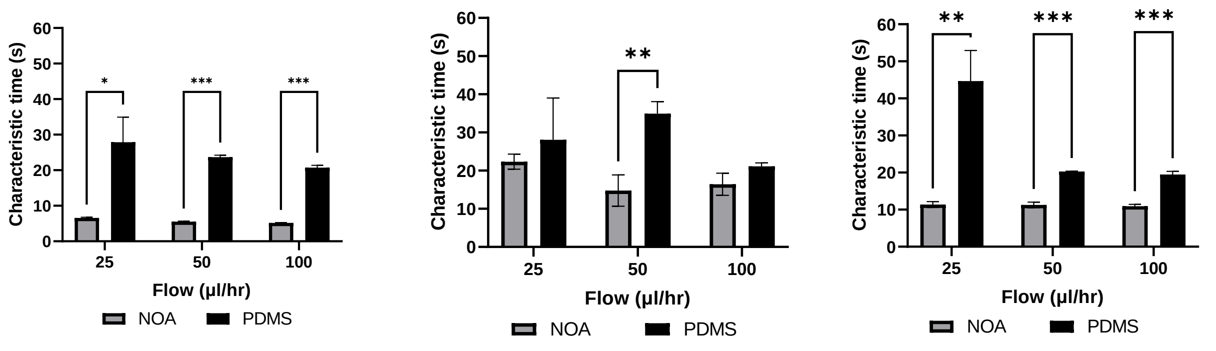

Chip A Chip B Chip C

**Figure 22: Comparing NOA and PDMS devices of chip A, B and C, average characteristic times at three different flow rates (25, 50, 100 in µL/h) of chip A (* *p*-value <0.05, ** *p*-value <0.01, *** *p*-value < 0.001).**

As shown in Figure 22, there is a significant difference between the characteristic times of the NOA device versus the PDMS device for all chips. For chip A, it was found that the PDMS devices had a characteristic time around 4 times longer than that of the NOA devices. At a flow rate of 25 µL/h, the PDMS device exhibited significantly longer characteristic times compared to the NOA device, which recorded times of 32.2 s and 7.7 s, respectively. For chip B, a significant difference was observed at a flow rate of 50 µL/h. At this flow rate, PDMS had a higher characteristic time than NOA of 34.9 s and 14.8 s, respectively. For chip C, a significant difference can be observed between PDMS and NOA devices at all flow rates. At a flow rate of 25 µL/h, PDMS had a higher characteristic time than NOA, of 44.7 s and 11.4 s, respectively. PDMS has on average a higher characteristic time than NOA devices of 4 times longer for chip A, 1.6 times longer for chip B and 2.5 times longer for chip C. The results presented in Figure 22 suggest a decay of characteristic time as the flow rates increased for all chips.

The statistical analysis revealed that the NOA devices provided more consistent results than the PDMS devices. Chip A showed standard deviations of ±0.38 µL/h, ±0.27 µL/h, and ±0.14 µL/h for flow rates of 25 to 100 µL/h. In comparison, the PDMS devices showed more inconsistency, showing standard deviations of ±12.2 µL/h, ±1.0 µL/h, and ±1.2 µL/h for the same flow rates of 25 to 100 µL/h. Similar trends can be observed for chips B and C.

### 3.1.4 Compliance

The compliance of all devices was found using the time characteristic extracted from Figure 21 and the experimental resistance from Table 6. The compliance found for each device at the different flow rates is presented in Figure 23.

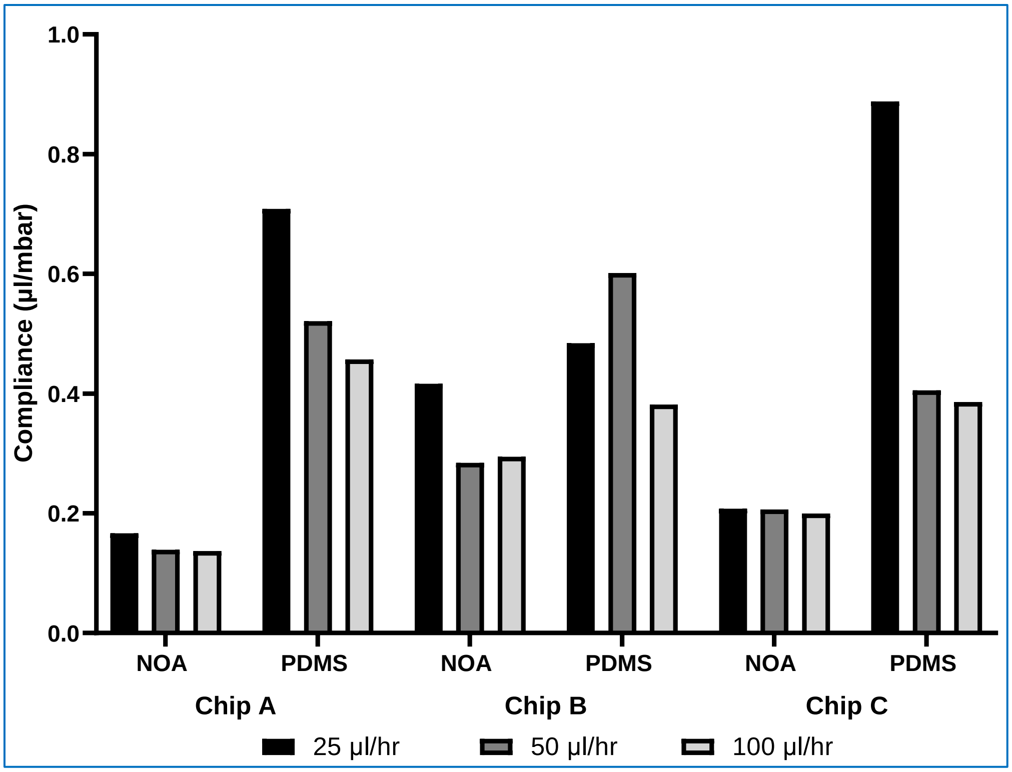

**Figure 23: Compliance from characteristic time of both NOA and PDMS chips A, B and C at the different flow rates (25, 50 and 100 µL/h).**

For both PDMS and NOA devices, chip A and chip C showed a decrease in the compliance as the flow rate increased. For chip A, PDMS showed a decrease in the compliance of 36%, while NOA showed a decrease of 18% from 25 µL/h to 100 µL/h. For chip C, PDMS showed a decrease in the compliance of 57%, while NOA underwent a decrease of 4% from 25 µL/h to 100 µL/h. For chip B, a decrease in the compliance could be observed as the flow rate increased for both NOA and PDMS devices, but at some flow rates there was an increase in the compliance.

An estimation of the compliance using the dimension of the channels can also be given as $C_l = \frac{V_{in}.a^2}{P}$, where $V_{in}$ is the initial volume, $a$ is the percentage by which the width increased, and $P$ is the pressure applied to flow in the channel. The relation of the compliance calculated from the volume as a function of the compliance found from the characteristic time is presented in Figure 24. All experimental outliers were removed.

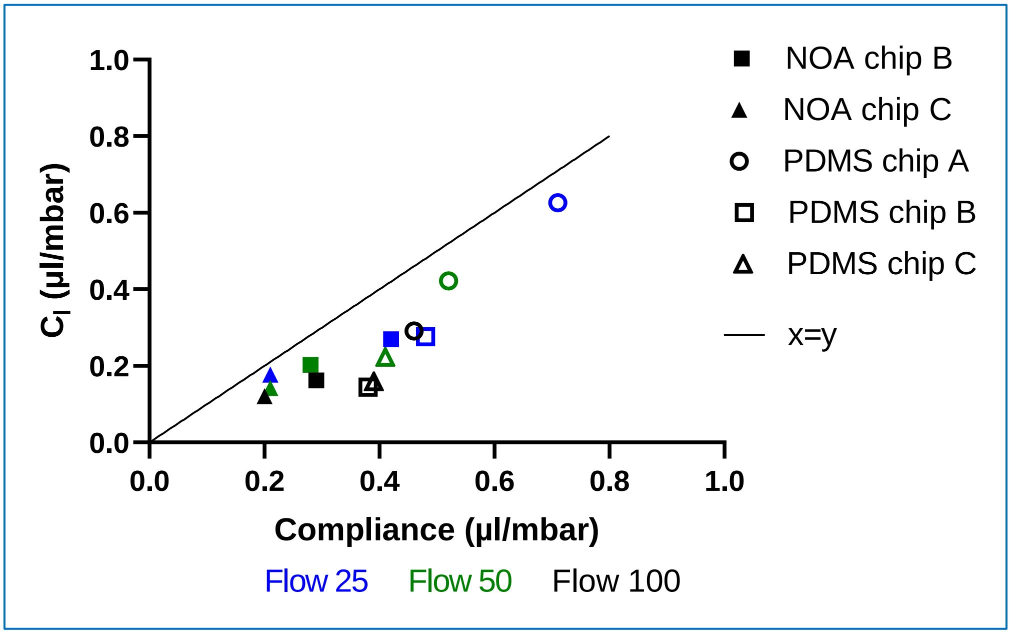

**Figure 24: Compliance from the channel deformation as a function of the compliance from the characteristic time ($\tau$) for all chips at flow rates 25, 50 and 100 µL/h.**

As shown in Figure 24, it can be observed that for all flow rates there is a correlation between the compliance from the channel's deformation and the compliance from the characteristic time, while $C_l$ seems underestimated.

## 3.2 Discussion

### 3.2.1 Surface Roughness and Young’s Modulus

The surface roughness can be found in Table 5. The mean arithmetic height and root mean square height are about 11 times higher for NOA63 than PDMS. This means that NOA63 has a rougher surface than PDMS. The Young’s modulus of the materials was found in Table 5. The PDMS has a Young’s modulus of 2.1 ± 0.2 MPa and the NOA63 has a Young’s modulus of 1743 ± 173 MPa. These values agree with those in the literature [25], [26], [27], [28]. NOA63 is more rigid than PDMS, which will allow less deformation of the channels under a constant flow rate, while it is a well-established fact that preparing PDMS with a 1:5 ratio increases its stiffness, resulting in a Young’s modulus of approximately 2.7 MPa [76]. This value remains significantly inferior to that of NOA, which is 800 times higher. This will lead to less compliance in the microfluidic devices. If a different type of Norland Optical Adhesive is used the Young’s modulus changes considerably (325 MPa for NOA81 compared to 1655 MPa for NOA63) [29].

### 3.2.2 Hydrophilicity/ Hydrophobicity of Surface

In Figure 20, a higher intercept, which is the initial pressure, can be observed for the NOA63 device than the PDMS. A higher initial pressure means that the chip is more hydrophobic. The contact angle measurement determines the hydrophilicity/hydrophobicity of the material surface. Both NOA63 and PDMS microfluidic devices received a plasma treatment. NOA63 presented a higher contact angle with plasma treatment (44.9° ± 3.1) and had a higher initial pressure (3.7 mbar) than the PDMS (32.1° ± 4.4 and 1.3 mbar). Therefore, NOA63 microfluidic devices are more hydrophobic than the PDMS.

### 3.2.3 Experimental Resistance

#### *3.2.3.1 Channels Width Deformation*

A difference between the channel widths of NOA63 and PDMS was observed in Figure 18. This difference can be explained by the double molding. The double molding decreases the average dimension, which explains the narrower width of the PDMS than the NOA [77].

Also, the difference between the resistance values of PDMS and NOA63 for each chip can be explained by the channel's width deformation. The propagation of error of the channel width was calculated to understand the effect of a difference in the channel's dimensions. Using a precision error of 0.5% for the width of the channels, the propagation error for chip A can be estimated at $1.24 \times 10^{13}$ Pa·s/m$^3$. Due to the channel's deformation measurement and error propagation, high sensitivity is achieved in the channel's width measurement for the calculation of the theoretical resistance. This can explain the difference between the experimental and theoretical values in Table 6.

#### *3.2.3.2 Dependency of Characteristic Time on Flow Rate*

Equation 19 presents the relation between the characteristic time, experimental resistance, and compliance. If the experimental resistance decreases, the characteristic time also decreases for a given compliance. As the flow rate increases, the characteristic time decreases due to lower compliance as observed in Figure 22 and Figure 23. PDMS microfluidic devices had a higher characteristic time for all chips and all flow rates compared to the NOA63 devices due to higher chip compliance.

NOA devices had a lower standard deviation than PDMS devices. This means that NOA devices have a better repeatability than PDMS devices. The high standard deviations might have occurred due to PDMS sensibility to small variations in material properties caused by temperature, holding time and ratio of polymer-curing agent [68], [78] , and the PDMS thickness that can affect the flow conditions due to deformation during use [26], [56], [79].

### 3.2.4 Compliance

As mentioned in Section 2.5.3.2, the characteristic time is related to the experimental resistance and the compliance. During the experiments, the same system setup was used with the same rigid tubing and glass syringe for all trials. The system setup material was assumed negligeable due to their low compliance and the resistance was assumed constant (measured value of $8.06 \times 10^{12}$ Pa·s/m$^3$). Hence, the difference in the experimental resistance and compliance can only be associated with the microfluidic chip [10]. Figure 23 demonstrates that PDMS devices a higher compliance than that of the NOA devices for all three chips. A negative correlation between compliance and flow rate has been observed. This indicates that compliance decreases as the flow rate increases. This phenomenon can be explained by the association of reduced deformability with an increase in channel width.

# 4 Evaluation of Hydraulic Resistance in Hexagonal Networks under Variable RBC Rigidity: Results and Discussion

In this chapter, the evaluation of the hydraulic resistance of the hexagonal networks under variable RBC rigidity are presented and discussed. This section explores how different concentrations of diamide in RBC at 10% HCT, which affect RBC circularity and deformability, impact hydraulic resistance. By measuring and comparing the resistance in hexagonal networks at various diamide concentrations in RBC, insights are gained into the relationship between RBC rigidity and flow resistance. The results highlight the nuanced interplay between cellular properties and microfluidic resistance, providing a deeper understanding crucial for optimizing microfluidic device performance in hemorheology research.

## 4.1 Results

### 4.1.1 RBC Circularity

The circularity of the RBC at 10% HCT with different concentrations of diamide has been measured using ImageJ as described in Section 2.4.2. The different images used for the measurement are presented in Figure 25. Table 7 summarizes the experimental and theoretical circularity of blood in different concentrations of diamide.

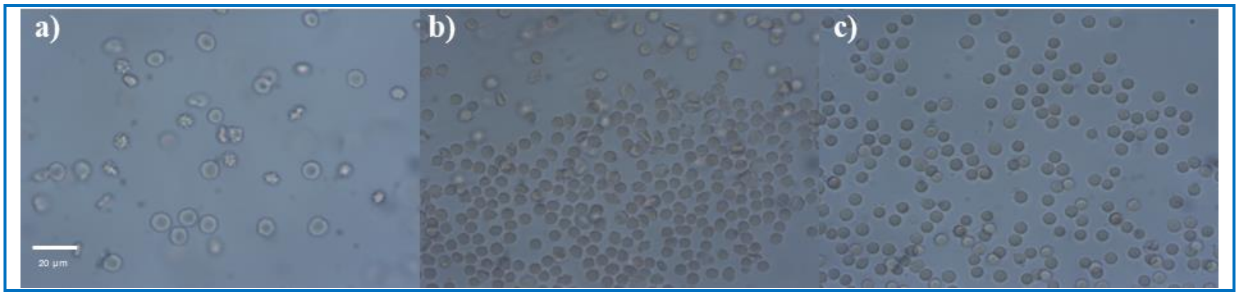

**Figure 25: Microscope images (63x) of the 10% HCT RBCs at different concentrations of diamide a) 0 µM, b) 50 µM and c) 200 µM**

**Table 7: Experimental circularity of RBCs and theoretical circularity of different concentrations of diamide. Circularity values range from 0 (irregular shape) to 1 (perfectly round shape).**

| Concentration of diamide (µM) | Circularity | Theoretical Circularity of RBC |
|---|---|---|
| 0 | 0.77 ± 0.14 | 0.635 ± 0.037 [80],<br>0.82 ± 0.01 [55] |
| 50 | 0.85 ± 0.03 | 0.82 ± 0.001 [55] |
| 200 | 0.92 ± 0.01 | 0.83 ± 0.02 [55] |

From Table 7, it can be observed that as the concentration of diamide increases, the circularity also increases which agrees with theoretical values.

### 4.1.2 RBC Deformation

The deformation of the RBCs has been measured using the ektacytometry and by fitting the data using the Lineweaver-Burk as described in Section 2.4.3. The figure below presents the elongation index as a function of the shear stress for RBC treated with different concentrations of diamide.

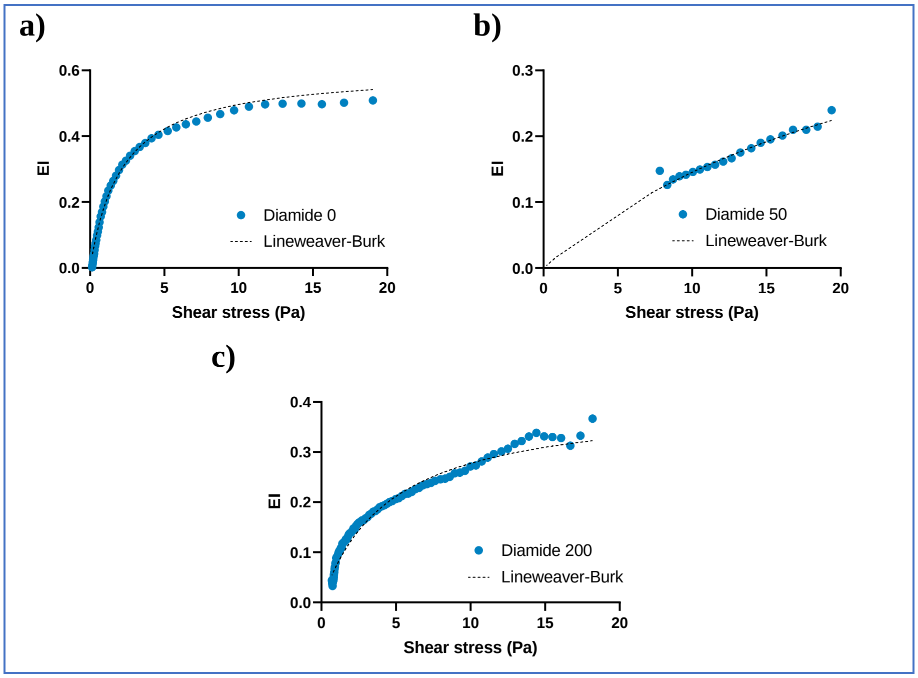

**Figure 26: Elongation index vs. shear stress for RBC treated with a) Diamide 0 µM, b) Diamide 50 µM and c) Diamide 200 µM. Lineweaver-Burk fits the data by using Equation 8 in order to determine max deformability ($EI_{max}$)and ½ shear stress.**

The table below summarizes the RBC maximum deformability (Elongation Index max ($EI_{max}$)) and the half shear stress (1/2 SS).

**Table 8: RBC max deformability ($EI_{max}$)and ½ shear stress for different concentrations of diamide (0, 50 and 200 µM)**

| Parameters | Diamide 0 µM | Diamide 50 µM | Diamide 200 µM |
|---|---|---|---|
| **$EI_{max}$** | 0.602 | 0.532 | 0.403 |
| **1/2 SS (Pa)** | 2.134 | 26.637 | 5.222 |

From Table 8, a decrease in the RBC max deformability can be observed as the concentration of diamide in RBC increases. For the half shear stress, RBC treated with Diamide 50 have a value that is higher than untreated RBC (Diamide 0) and RBC treated with Diamide 200.

### 4.1.3 Resistance Estimation

The hydraulic resistance of the hexagonal network for RBC treated with different concentrations of diamide were found by following the dual pressure controlled setup from Section 2.5.1.2 and analyzed using the experimental hydraulic resistance estimation procedure described in Section 2.5.2.1. Since the experimental resistance of the tubing is $6.08 \cdot 10^{12}$ $Pa \cdot s/m^3$, which is 100 time smaller than the hydraulic resistance of the chip, it was considered negligible.

A calibration of the hexagonal networks is done using an OptiPrep-PBS-Glucose solution. To avoid cross-contamination between RBC treated with different concentrations of diamide, a new chip is used for each concentration. This is why a calibration line is necessary for each concentration of diamide in every hexagonal network. The pressure-flow rate data of the calibration is presented in Figure 27.

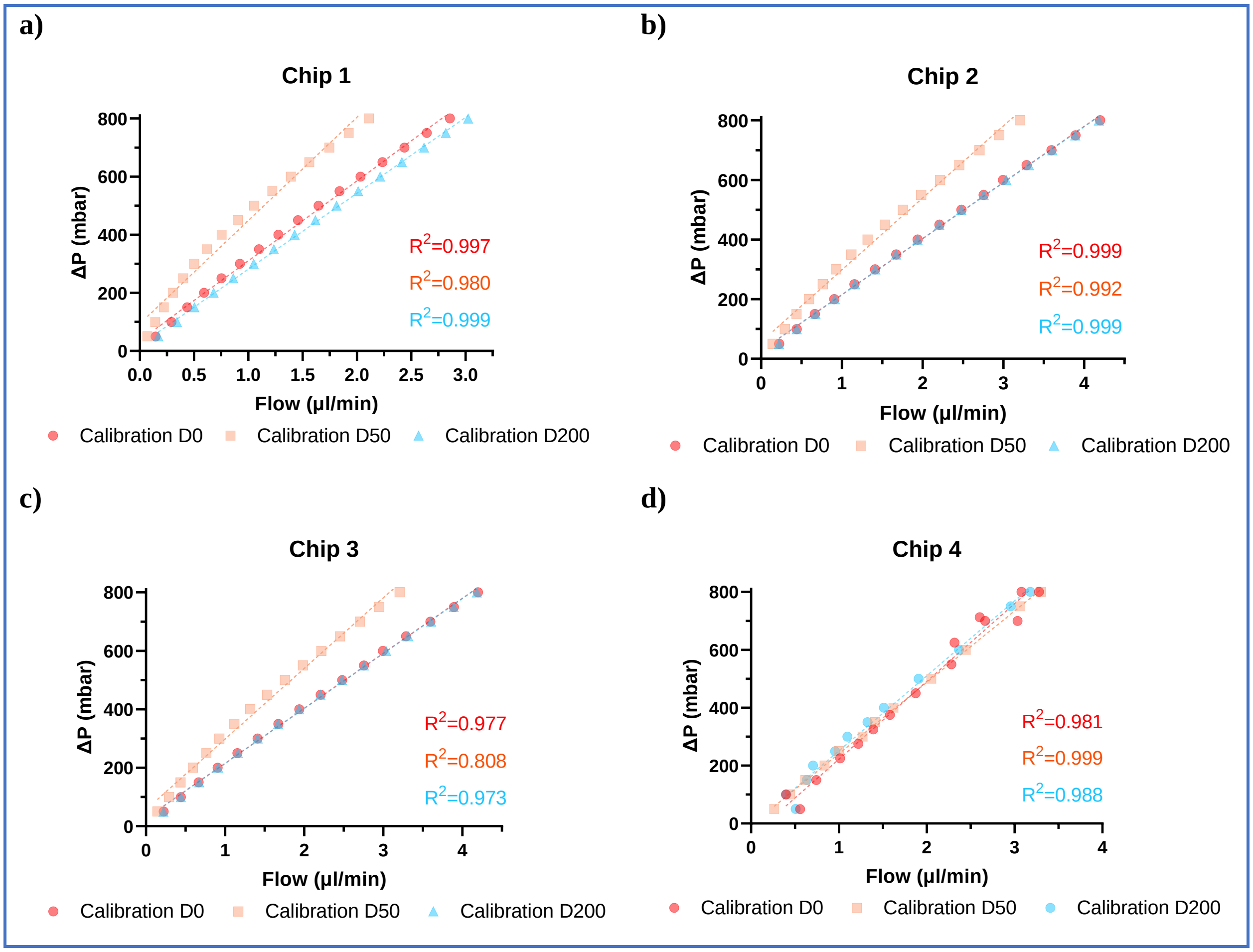

**Figure 27: Pressure-flow rate relation of the calibration test at each concentration of diamide for a) Chip 1, b) Chip 2, c) Chip 3 and d) Chip 4**

For Calibration D50, Chip 1, Chip 2, and Chip 3 exhibit the highest hydraulic resistance and show non-linearity due to the compliance of the chips. In contrast, Calibration D0 and D200 maintain consistent hydraulic resistance across all four hexagonal networks and demonstrate high linearity ($R^2$>0.95). The same chip was utilized for calibration D0, D50, and D200, and the same pressure-flow rate relationship was observed, which demonstrates the repeatability of the data acquisition process.

The variations of pressure as a function of the flow rate of the four hexagonal chips are presented in Figure 28 and in Figure 29. Figure 28 presents the pressure-flow rate relation of the four hexagonal networks for RBC treated with different concentrations of diamide. While Figure

29 presents the same pressure-flow rate data results of blood at 10%HCT treated with different concentrations of diamide for each chip.

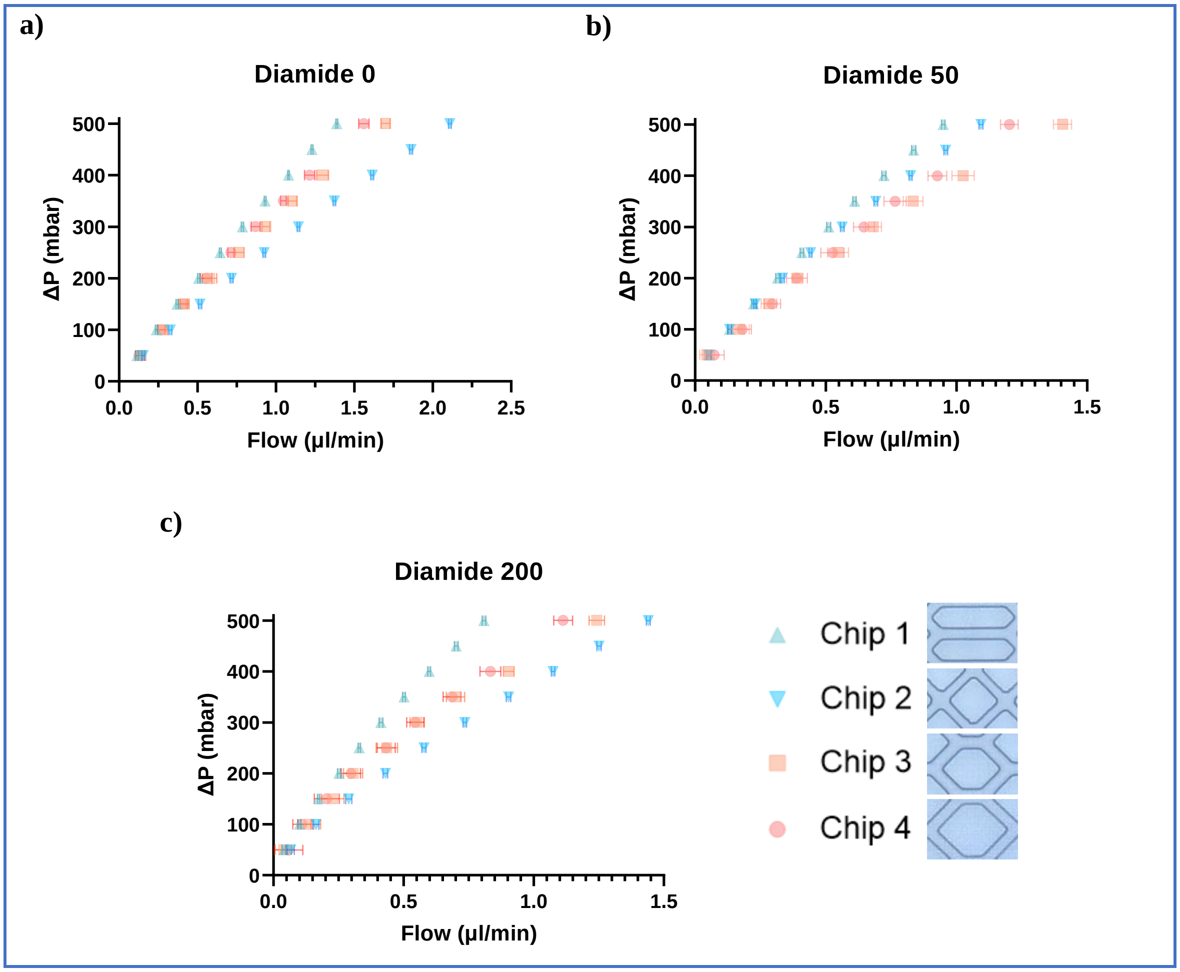

**Figure 28: Pressure-flow rate plots of the four hexagonal networks of blood at 10% HCT treated with a) 0 µM diamide b) 50 µM diamide and c) 200 µM diamide of the four hexagonal networks.**

Let's recall that chips were designed to have the same theoretical resistance with a Newtonian fluid. Therefore, any differences that arise are due to the complexity of blood. At 500 mbar, a difference of the flow rate for all chips can be observed. This signifies that the resistance at 500 mbar varies for the different chips. For untreated RBC at 10% HCT (Diamide 0), Chip 2 has the lowest resistance, Chip 3 has a slightly smaller resistance than Chip 4 and Chip 1 has the highest resistance as seen in Figure 28. For RBC treated with Diamide 50, Chip 3 has a slightly smaller resistance than Chip 4, followed by Chip 2 and Chip 4. For RBC treated with Diamide 200, the same resistances can be observed as for untreated RBC (Diamide 0).

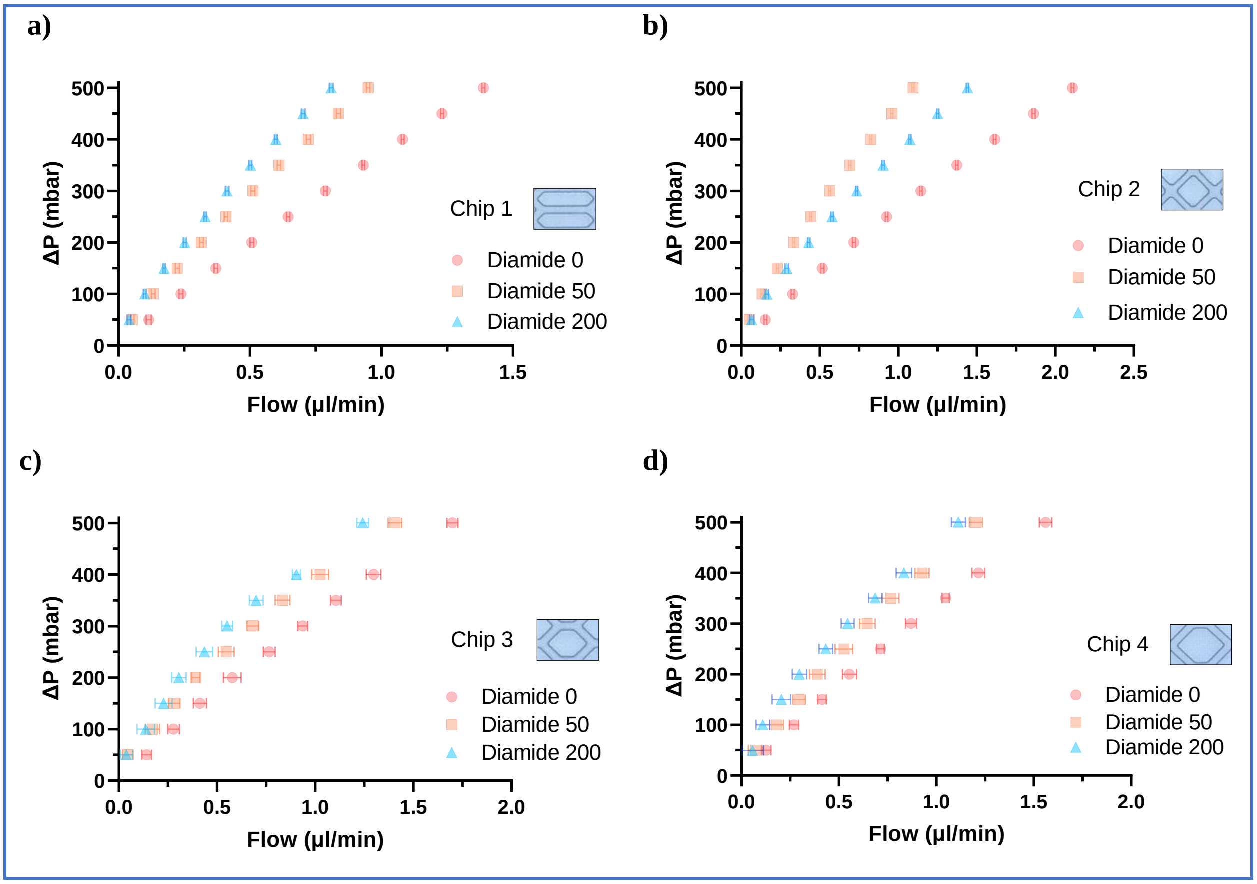

**Figure 29: Pressure-flow rate plots of RBCs at 10% HCT treated with 0, 50 and 200 µM diamide for a) Chip 1, b) Chip 2, c) Chip 3 and d) Chip 4.**

Figure 29 presents the pressure and flow rate relation of the four hexagonal chips with RBC at 10% HCT at different concentrations of diamide. For Chip 1, Chip 3 and Chip 4, there is an increase in the resistance as the concentration of diamide in RBC at 10% HCT increases at a pressure of 500 mbar. For Chip 2, the RBC treated with Diamide 50 has a higher resistance than the RBC treated with Diamide 200.

The characteristic experimental resistance was estimated using the pressure data at ≈500 mbar with the associated flow rate at each concentration of diamide in RBC for the four hexagonal networks. This pressure was chosen because it produces the greatest difference in flow rate between the various diamide concentrations across all hexagonal networks. Also, the slopes of the different linear correlations in Figure 27 are the hydraulic resistances of the calibration solution at each concentration of diamide for each hexagonal network. Table 9 presents the experimental resistance of RBC treated with different concentrations of diamide, the theoretical resistance and the calibration resistance. The theoretical resistance of each device is determined by calculating the hydraulic resistance of each channel, whether arranged in parallel or series, using the appropriate hydraulic resistance equations for rectangular, circular, and tapered channels as seen in Table 1 with a viscosity of 3.5 cP (assumed viscosity of blood).

**Table 9: Experimental hydraulic resistance and theoretical hydraulic resistance of the four hexagonal networks and PBS solutions.**

| **Hydraulic Resistance ($10^{15}$ Pa·s/m$^3$)** | **Hexagonal Networks** | | | |
|---|---|---|---|---|
| | **Chip 1** | **Chip 2** | **Chip 3** | **Chip 4** |
| **Diamide 0 µM** | 2.16 | 1.53 | 1.76 | 1.92 |
| **Diamide 50 µM** | 3.16 | 3.04 | 2.14 | 2.49 |
| **Diamide 200 µM** | 3.71 | 2.32 | 2.42 | 2.70 |
| **Calibration D0** | 1.65 | 1.13 | 1.53 | 1.61 |
| **Calibration D50** | 2.13 | 1.45 | 1.66 | 1.48 |
| **Calibration D200** | 1.57 | 1.13 | 1.50 | 1.55 |
| **Theoretical** | 2.03-3.35 | 3.23-5.33 | 1.97-3.59 | 2.11-3.48 |

The resistance of the calibration solution is used to normalize the resistance values obtained from the experimental data for the RBC treated with different concentrations of diamide. The normalized resistance which represents the relative apparent viscosity was calculated by comparing the resistance values from 10% hematocrit (HCT) samples treated with various diamide concentrations to those from its associated calibration solution and presented in Figure 30. This was achieved using the formula: $\left(Normalized\ R = \frac{R_{diamide}}{R_{Calibration}} = \frac{\Delta P_{diamide}}{Q_{diamide} \cdot R_{Calibration}} = \frac{\mu_{diamide}}{\mu_{calibration}}\right)$.

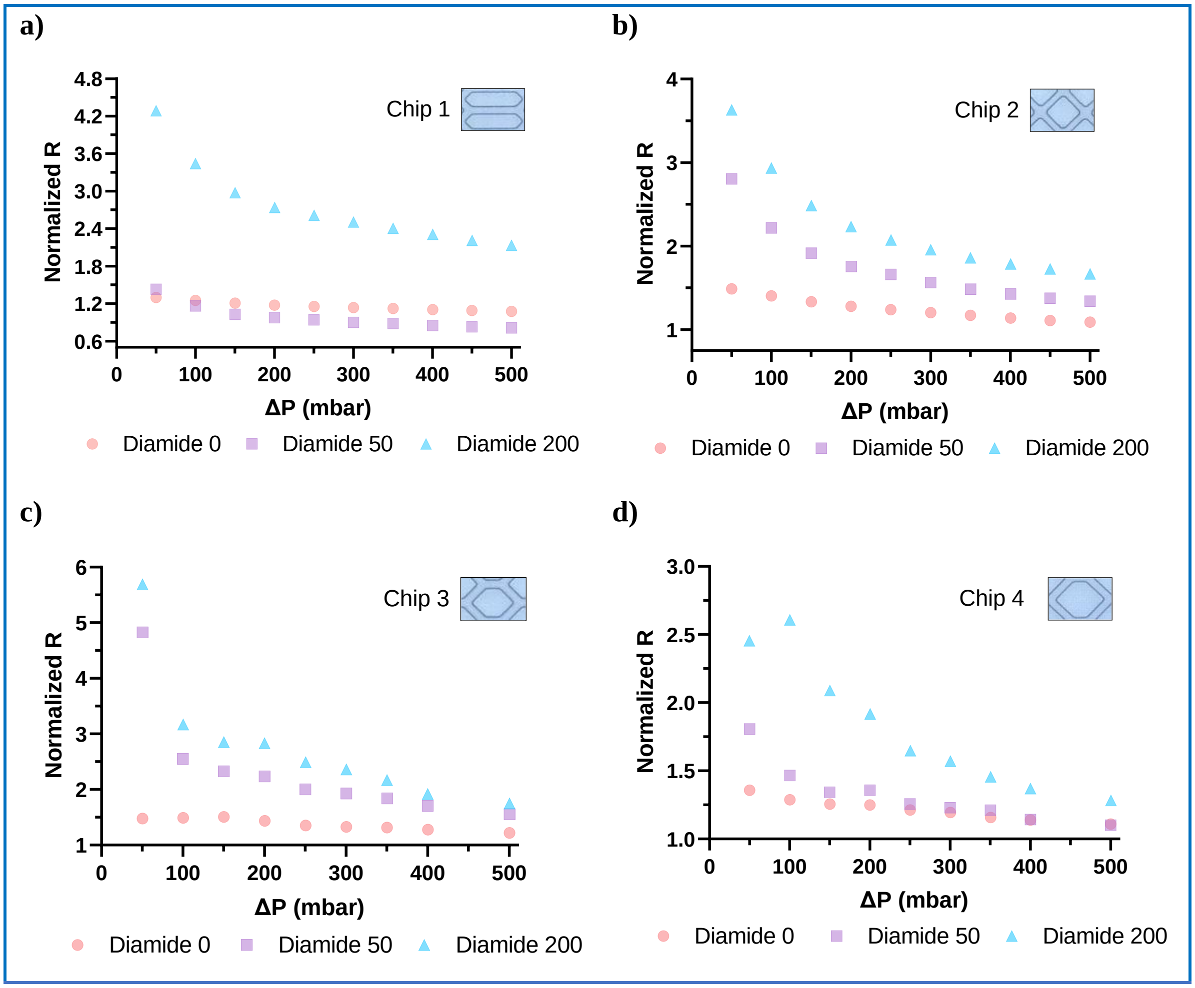

**Figure 30: Normalized resistance as a function of the variation of pressure at 10% HCT with 0, 50 and 200 µM diamide for a) Chip 1, b) Chip 2, c) Chip 3 – Test 1, d) Chip 3 – Test 2 and e) Chip 4.**

In Figure 30, the curves for RBC treated with each concentration of diamide are non-linear which is normal for non-Newtonian fluids. Also, it can be observed that there is an increase in the normalized resistance as the concentration of diamide in RBC increases for all the chips at a variation of pressure of 50 mbar. As the pressure increases the normalized resistance stabilized around 1-2 depending on the chip and concentration. For Chip 1, it can be observed that for a pressure higher than 100 mbar, RBC treated with Diamide 50 have a lower normalized resistance than RBC treated Diamide 0.

## 4.2 Discussion

### 4.2.1 Effect of RBC Deformation on Experimental Resistance

As shown in Figure 29, the characteristic resistance of each concentration of diamide in 10% HCT for each hexagonal network was estimated for ΔP≈ 500 mbar and presented in Table 9. It was found that the resistance increased with the different concentrations of diamide in RBC for the four hexagonal networks. This was expected because diamide is known to rigidify the red blood cells [55], [81]. Rigidification of the membrane leads to less flexibility of the cells meaning that they deform less. This can be confirmed by the ektacytometry test where it was found that the RBCs treated with higher concentration of diamide deform less (Table 8).

A variation of the flow rate between the different hexagonal networks for the different concentrations of diamide in 10% HCT can be observed at 500 mbar. This means that the resistance (ΔP/Q) is different depending on the geometry of the hexagonal networks when a complex fluid is flowing through the network (Table 9). Chip 1 has more elongated hexagons while Chip 2 is shaped as a square. From that, we can see that a network with more elongated hexagons corresponds to higher resistance while network with squared shaped corresponds to lower resistance for all concentrations of diamide at 500 mbar. Chip 3 and Chip 4 have similar hexagonal shapes, and their hydraulic resistance is almost equal for all concentrations of diamide in 10% HCT at the same pressure. Therefore, the geometry of the channels influences the hydraulic resistance when blood at 10% HCT treated with different concentrations of diamide flows through the networks. This also signifies that the geometry of the network is sensitive to the deformation of RBC. This provides interesting information for the optimization of microfluidic design in microcirculation and for the study of RBC deformation.

Figure 30 shows the normalized resistance over the pressure. At 50 mbar, an increase in the normalized resistance can be observed as the concentration of diamide in 10% HCT increases. This was expected since it was observed that the red blood cells are more spherical and therefore more rigid (less deformation) as the concentration of diamide in RBC increases (Table 7 and Table 8). As the pressure increases, a decrease in the normalized resistance can be observed. This was expected due to the blood shear-thinning behaviour. At higher pressure (≥ 200 mbar), the normalized resistance stabilizes around values of 1-2 depending on the concentration of diamide and the hexagonal network. Since the calibration linear correlation presented in Figure 27 have a very good fit of the regression model ($R^2>0.97$), we can affirm that the system operates in a non-compliant regime. As a result, the decrease in the normalized resistance as the pressure increases is due to the RBC deformation. Therefore, the stabilized value of the normalized resistance is determined by the ratio of the blood viscosity to PBS.

### 4.2.2 Clinical Applications

In this study, the RBC deformation was not measured using the hexagonal networks, but only with the ektacytometry. The images taken with the high-speed camera by my colleague Andy Le can track the RBC in the hexagonal network. From these images, the deformation of RBC in the hexagonal networks can be extracted. Since the networks are sensitive to RBC deformation as discussed above, both ektacytometry and microfluidics offer the possibility of studying RBC deformation. In the Piety *et al.* study, they compared the RBC deformation results from the ektacytometry to those of microfluidic devices [82]. It was found that ektacytometry did not provide as precise measurement as the microfluidic devices for the estimation of RBC deformation

[82]. This provides a pathway for the consideration of microfluidic devices for the monitoring of blood diseases that influence the RBC rigidity such as diabetes and sickle cell anemia.

The hemodynamic response in the hexagonal networks is multifactorial and depends on the properties of blood cells and the geometry of the network as discussed previously. This discovery paves the way for a better understanding of the circulatory physiology networks in the body, which present themselves in very different ways in various organs. This also raises the question of why these differences exist and how they affect blood circulation and overall health.

The setup provided in this experiment can provide a good understanding of the blood dynamics in very small vessels for the study of hemorheology due to the use of a dual pressure setup. Using a pressure driven setup is important to imitate physiological characteristics. Furthermore, by stiffening the RBC using a chemical agent like diamide, many cardiovascular diseases (diabetes) and hematological disorders (hereditary spherocytosis) can be studied to better understand the blood flow in the microcirculation for the development of drugs [81].

# 5 Collaborative Research on Retina Networks for Hydraulic Resistance Studies: Results and Discussion

This chapter investigates the hydraulic resistance within a retinal microvascular network, focusing on the effect of various fluid viscosities. The analysis includes a viscosity test and a pressure-flow rate control to evaluate how different fluids, such as blood and glycerol solutions of varying concentrations, influence the hydraulic resistance within the retinal channels. This study aims to provide insights into the behavior of blood flow in microvascular networks, which is crucial for understanding microcirculatory pathologies and developing therapeutic strategies.

## 5.1 Results

### 5.1.1 Viscosity

The viscosity of the different concentrations of glycerol was obtained using a viscosimeter (Section 2.3.5). The table below presents the experimental and theoretical viscosities of the different concentrations of glycerol.

**Table 10: Experimental and literature viscosity of the different concentrations of glycerol**

| Concentration of glycerol | Test | Experimental Viscosity (mPa·s) | Average Experimental Viscosity (mPa·s) | Literature Viscosity (mPa·s) |
|---|---|---|---|---|
| 0.4 | 1 | 4.26 | 4.21 ± 0.03 | 3.42-3.63 [83], [84] |
| | 2 | 4.21 | | |
| | 3 | 4.17 | | |
| 0.6 | 1 | 4.78 | 4.76 ± 0.02 | 9.17-11.67 [83], [84] |
| | 2 | 4.71 | | |
| | 3 | 4.78 | | |
| 0.8 | 1 | 18.82 | 22.36 ± 1.81 | 46.3-48.79 |
| | 2 | 23.49 | | |
| | 3 | 24.77 | | |

The results show an increase in the average viscosity as the concentration of glycerol increases. The average experimental viscosity found do not agree with the literature [83], [84].

### 5.1.2 Resistance Estimation

The hydraulic resistances of the retina network for different fluids (RBC at 20% HCT, 0.4, 0.6 and 0.8 glycerols) were found by following the procedure for a single pressure-controlled setup (Section 2.5.1.1) and analyzed using the experimental hydraulic resistance estimation procedure described in Section 2.5.2.1. The pressure as a function of the flow rate for the whole system (with the chip) and without the chip was plotted for each of the fluids in Figure 31.

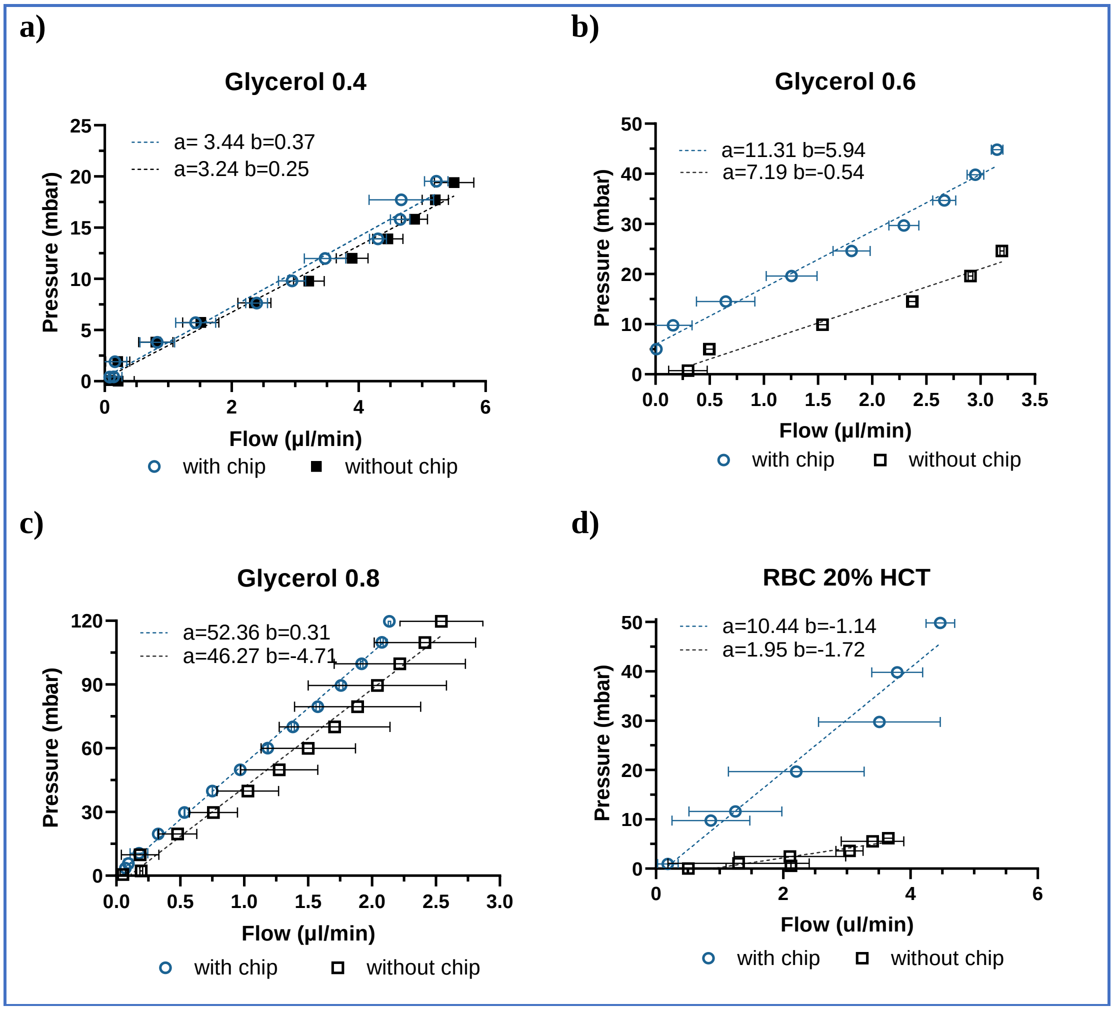

**Figure 31: Pressure as a function of the flow rate with and without the chip for a) glycerol 0.4, b) glycerol 0.6, c) glycerol 0.8 and d) RBC 20% HCT. For all fluids, with and without chip, n=3.**

The linear slopes (a-value) on the plots in Figure 31 represent the experimental hydraulic resistance for each fluid with and without the chip while the b-value represents the intercept. By subtracting the values of the linear slope, as shown in Equation 10, the experimental resistance of only the chip can be extracted. The experimental hydraulic resistance and the theoretical hydraulic resistance are presented in Table 11.

To calculate the theoretical resistance, Equation 1 has been used with $\Delta P$ being the intraocular pressure (IOP), and Q the blood flow rate obtained from Julien's simulations [62]. The range of the theoretical resistance has been calculated with $\Delta P=[9:18]$ mmHg and $Q = [3.75:62.1]$ µl/min [62].

**Table 11: Experimental hydraulic resistance and theoretical hydraulic resistance of the retina network with different fluids**

| Fluid | Experimental resistance ($10^{13}$ Pa·s/m$^3$) | Theoretical resistance ($10^{13}$ Pa·s/m$^3$) |
|---|---|---|
| Glycerol 0.4 | 0.12 | 0.12-3.84 |
| Glycerol 0.6 | 2.47 | 0.35-11.6 |
| Glycerol 0.8 | 3.65 | 1.60-52.9 |
| Blood 20%HCT | 5.16 | 0.16-3.84 |

Figure 32 presents the relation of pressure-flow rate within the retina network for the different fluids for the whole system of one experiment for the whole chip (chip with tubings).

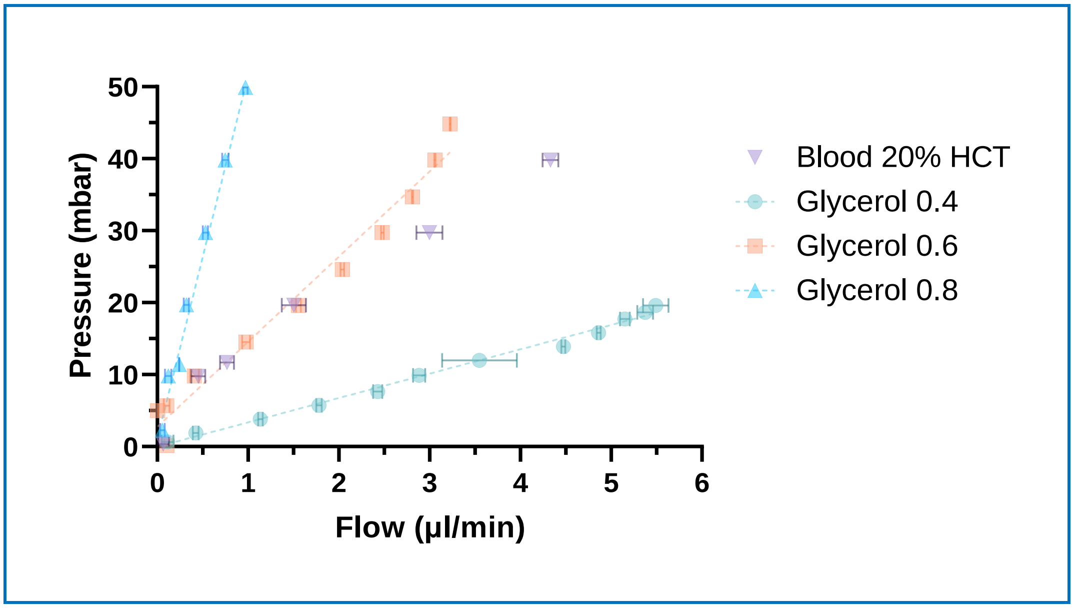

**Figure 32: Relation of pressure-flow rate for the different fluids for n=1 of with chip data.**

Figure 32 shows a linear correlation between the pressure and flow rate for the different concentrations of glycerol. In contrast, blood at 20% HCT does not have a linear correlation. Also, a higher initial pressure was needed for blood with a hematocrit of 20% compared to the various glycerol concentrations (0.4, 0.6, and 0.8). Specifically, the initial pressure required for blood was 10.93 mbar, while for glycerol it was 0.12 mbar, 6.48 mbar, and 5.02 mbar, respectively.

## 5.2 Discussion

### 5.2.1 Effect of Fluid Viscosity on Experimental Resistance

From Figure 32, it was observed that water-glycerol mixture presented a linear correlation as expected for Newtonian fluids due to viscous changes. On the other hand, blood at 20% HCT presented a non-linear correlation. This suggests that the PDMS chip used in the experiment is operating in a non-compliant regime, where any non-linearity in the results can be attributed to the properties of the fluid being tested. Furthermore, there is an increase in the hydraulic resistance as the concentrations of glycerol increases which is normal because the resistance is dependent on the viscosity of the fluid as seen in the Hagen-Poiseuille model. The experimental resistance of the network for all glycerols was in the range of the theoretical resistance as shown in Table 11. This means that the proposed setup provides accurate measurements of the pressure and flow rate. Compared to the theoretical resistance, blood experimental resistance was higher. Blood is a non-Newtonian fluid and behaves as a shear thinning fluid. This means that the viscosity decreases as the shear rate increases. This is caused by the complex nature of blood due to the deformability of the RBC and uneven distribution of the cells [8].

Also, it was noticed that blood at 20% HCT required a higher initial pressure to overcome the resistance of the channel than the different concentrations of glycerol. This means that the chip was more hydrophobic when blood was used. This was also found in a previous study by Pitts *et al.* [85]. This is important because the retina networks can be clogged and therefore affect the results of the relation between the pressure-flow rate.

### 5.2.2 Clinical Applications

The retina network has great potential for hemorheology studies. The network can be used at low pressure and flow rate to imitate physiological parameters to characterize blood microcirculation. This can lead to better understanding and drug development for cardiovascular diseases such as hypertension and diabetes. These diseases are also related to retina anomalies such as the retinopathy [41].

# 6 General Discussion

This chapter discusses the device uncertainties and compares the different pressure-controlled setups. This provides a comprehensive understanding for optimizing microfluidic system design and performance.

## 6.1 Comparison of the Pressure Controlled Setups

This study introduced two pressure-controlled setups. The single-controller setup yielded accurate and reliable measurements of hydraulic resistance in tapered-parallel networks and the retina, using both water and glycerol. However, this setup had a higher standard deviation for the measurement of the flow rate. This is probably caused by the assumption that the pressure at the system's exit is zero. This can lead to less precise pressure variations. On the other hand, the dual pressure controllers had a lower standard deviation for the measurement of the flow rate in the hexagonal networks. However, higher pressure was used with the dual pressure controller than the single pressure controller. Overall, the proposed pressure-controlled setups delivered precise results across various network configurations, underscoring their potential for reliable further use.

## 6.2 Devices Uncertainties

### 6.2.1 Flow Rate Measurement Uncertainty

The Fluigent flow meter S used has a flow rate range of ±7 µL/min. For water, the accuracy of the device was ±5% of the measured value for flow rates higher than 0.42 µL/min and ±0.021 µL/min for measurements below 0.42 µL/min. The repeatability of the device was within 0.5% for all measurements taken above 42 µL/h and ±0.21 µL/h below 42 µL/h. Hence, the taken measurements of the flow rate for the tapered-parallel networks, hexagonal networks and retina network were repeatable within 0.5% of the measured value. This indicates that the Fluigent flow meter S is an excellent device that can be used to measure the flow rate in microfluidic devices.

### 6.2.2 Pressure Controller Measurement Uncertainty

The Flow EZ pressure controller has a resolution of 0.03% of the maximum pressure. In Section 2.5.1.1, the Flow EZ 2000 mbar has been used and in Section 2.5.1.2 the Flow EZ 1000 mbar has been used. Therefore, the pressure controller can measure pressures as small as 0.6 mbar and 0.3 mbar respectively. The measured values of all networks are in this range. The device stability is 0.1% on the measured value which is effective beyond 10% of the maximum pressure. The device demonstrates effective stability for pressures up to 1200 mbar and 1100 mbar, respectively. Beyond these values, stability decreases, leading to less consistent and accurate results. Additionally, the device offers a low response time of 30 ms, which is critical for applications requiring real-time pressure monitoring and control.

### 6.2.3 Anticipated Periodic Instability of the Output Flow

The results presented in Figure 21 present the flow rate over time of both PDMS and NOA devices at different flow rates. The two-element model data measurements show a clear rise and a plateau with a sinusoidal behaviour for NOA and PDMS devices [10]. This behaviour was found to be caused by the syringe pump’s stepper motor (Nexus 3000, Chemyx, Stafford, TX, USA)[10], [86], [87].

# 7 Conclusion

## 7.1 Summary

The hemodynamic response in microfluidic devices is multifactorial and depends on the blood cell properties, the geometry of the network and the vessel's compliance. Due to blood complexity, hemorheology studies in microcirculatory networks are still in a development stage and there is a need to develop new methodologies and technologies to advance our understanding. The scope of this thesis was to present an experimental setup that can assess the hydraulic resistance of different microfluidic devices made of different materials (PDMS and NOA), different geometries (tapered-parallel networks, hexagonal networks and retina network) and different fluids (water, glycerol and blood) to optimize microfluidic chip designs and for hemorheology research. The scope was achieved by answering three objectives with three projects.

The research comprised three main objectives: (1) characterizing the mechanical properties of PDMS and NOA, (2) quantifying compliance under flow conditions in microfluidic networks, and (3) analyzing the pressure-flow rate relationship to estimate hydraulic resistance in different geometries. To achieve these objectives, three projects were performed. The first project investigated the mechanical and hydraulic properties in tapered-parallel networks The mechanical properties of PDMS and NOA devices were assessed attaining the first objective. It was found that NOA devices have a rougher surface, deform less under pressure, are more hydrophobic when treated with plasma, and possess a tensile strength approximately 800 times higher than PDMS devices. Additionally, the compliance of tapered-parallel networks was measured by determining the characteristic time under repeatable flow rate conditions achieving the second objective. The results indicated that the characteristic times for chip A were, on average, four times longer for PDMS devices than NOA devices, 1.6 times longer for chip B, and 2.5 times longer for chip C.

These findings demonstrate that NOA microfluidic devices are less compliant than PDMS devices and suggest that NOA devices could enhance consistency in microfluidic research due to their significantly lower standard deviations. The hydraulic resistance of the microfluidic device was found for all three chips of both PDMS and NOA reaching the third objective. It was found that PDMS had a higher percentage of error in the hydraulic resistance due to a higher channel deformation which also led to higher compliance. The results provide insights of a less compliant material that can be used for optimizing microfluidic devices in biomedical engineering.

The second project focused on quantifying the experimental hydraulic resistance of four hexagonal networks. Using a dual pressure-controlled setup, it was found that the experimental resistance, the circularity and deformation increased with the rigidity of red blood cells (RBCs). As the concentration of diamide increased, the RBCs deformed less while flowing through the small channels, requiring higher pressure and flow rate to pass through. This project fulfilled the third objective by demonstrating how the mechanical properties of RBCs influence the hydraulic resistance within hexagonal networks, providing valuable insights into the behavior of blood under different conditions advancing hemorheology research.

The third project aimed to quantify the experimental hydraulic resistance of retina networks using fluids of different viscosities. Three concentrations of glycerol were used to illustrate the behavior of Newtonian fluids, showing a linear correlation with resistance increasing proportionally to glycerol concentration (0.4, 0.6, and 0.8). For blood at 20% HCT, the experimental resistance was higher than theoretical predictions and showed a non-linear behviour, likely due to blood's complex nature, uneven distribution, and cell deformability. The non-linearity of blood which is a non-Newtonian fluid and the linearity of glycerols which are Newtonian fluids, provide evidence that the retina network is operating in a non-compliant regime. This means that the pressure-flow rate results can be attributed to the properties of the fluid being tested achieving the second objective. This project completed the third objective by providing accurate and reliable resistance data for different networks, contributing to advancements in microfluidic and microvascular research.

The three projects' methodology fulfilled the scope of this research of optimizing microfluidic devices for hemorheology research by presenting accurate and reliable results. Furthermore, the proposed methodology presents a potential contribution for physio-pathological comprehension of vascular diseases, for the development of lab-on-chip devices and for more accurate mathematical models for the simulation of blood flow in microcirculatory networks where flow control, device performance and understanding of blood behaviour are necessary. Ultimately this research could lead to the development of more targeted and effective treatments for specific diseases such as micro-stenosis and the impairment of microcirculatory density.

## 7.2 Future Work

The development of biomimetic chips with physiological compliance is crucial for conducting more precise *in vitro* studies of the hemodynamic response in microcirculatory networks. By studying the impact of disease-specific microcirculation geometry, such as stenosis and impairment of microcirculatory density, we can better understand the factors that contribute to the hemodynamic response. Comparing the pressure losses in microcirculatory networks of different organs can also provide valuable insights into the impact of geometry on blood circulation and organ physiology. The proposed *in vitro* methodology in this study can be utilized to investigate the hemodynamic response in pathological conditions, such as inflammation and thrombosis. Additionally, the development of more accurate mathematical models for the simulation of blood circulation in microcirculatory networks can greatly benefit from the integration of the multifactorial factors (pressure, flow rate, resistance and compliance) identified in this study.

The retinal microvascular network used in this research offers a unique opportunity to study microvascular diseases due to its association with diseases like hypertension, diabetes, arterial stenosis and strokes. For future work, the development of the microcirculatory network models with levels of compliance and resistance that faithfully replicate those observed *in vivo* should be focused on the retina network. This process entails appropriate material selection and utilizing medical images to achieve geometry matching physiological or pathological characteristics. Subsequently, to characterize the underlying causes of retinal diseases, the measurement of the apparent viscosity using the pressure-flow rate measurement method while observing red blood cell behaviour using videomicroscopy needs to be accomplished. This approach will enable to determine red blood cell deformation and local density, thereby characterizing their role in the pathophysiological changes of retinal microcirculation. By doing this analysis, the aim is to pave the way for advancements and contribute to the development of treatments for cardiovascular diseases. This research has the potential to enhance the detection and treatment of ocular disorders while sharing crucial data on microcirculation beneficial to the hemodynamics community. These data will exert influence beyond the initial scope of the project.

# References

[1] E. K. Sackmann, A. L. Fulton, and D. J. Beebe, “The present and future role of microfluidics in biomedical research,” *Nature*, vol. 507, no. 7491, pp. 181–189, Mar. 2014, doi: 10.1038/nature13118.

[2] E. Y. Song, D. Cheng, and L. Zhao, *Fundamentals, Devices and Applications*. Weinheim, Germany: Wiley, 2018.

[3] G. M. Whitesides, “The origins and the future of microfluidics,” *Nature*, vol. 442, no. 7101, pp. 368–373, Jul. 2006, doi: 10.1038/nature05058.

[4] T. Quires and S. Quake, “Microfluidics: Fluid physics at the nanoliter scale,” *Rev. Mod. Phys.*, vol. 77, no. 3, pp. 977–1026, Oct. 2005, doi: 10.1103/RevModPhys.77.977.

[5] H. A. Stone, A. D. Stroock, and A. Ajdari, “Engineering Flows in Small Devices: Microfluidics Toward a Lab-on-a-Chip,” *Annu. Rev. Fluid Mech.*, vol. 36, no. 1, pp. 381–411, Jan. 2004, doi: 10.1146/annurev.fluid.36.050802.122124.

[6] D. Mark, S. Haeberle, G. Roth, F. von Stetten, and R. Zengerle, “Microfluidic lab-on-a-chip platforms: requirements, characteristics and applications,” *Chem. Soc. Rev.*, vol. 39, no. 3, pp. 1153–1182, Feb. 2010, doi: 10.1039/B820557B.

[7] O. K. Baskurt and H. J. Meiselman, “Erythrocyte aggregation: Basic aspects and clinical importance,” *Clin. Hemorheol. Microcirc.*, vol. 53, no. 1–2, pp. 23–37, Jan. 2013, doi: 10.3233/ch-2012-1573.

[8] E. Nader *et al.*, “Blood Rheology: Key Parameters, Impact on Blood Flow, Role in Sickle Cell Disease and Effects of Exercise,” *Front. Physiol.*, vol. 10, p. 1329, Oct. 2019, doi: 10.3389/fphys.2019.01329.

[9] A. S. Popel and P. C. Johnson, “Microcirculation and hemorheology,” *Annu. Rev. Fluid Mech.*, vol. 37, pp. 43–69, 2005, doi: 10.1146/annurev.fluid.37.042604.133933.

[10] Armstrong, Curtis J.K., “Red Blood Cell Aggregation Characterization Using Norland Optical Adhesive Microfluidic Chips for a Reduction in Compliance,” Thesis, University of Ottawa, Ottawa, Canada, 2020. Accessed: Mar. 12, 2024. [Online]. Available: https://ruor.uottawa.ca/server/api/core/bitstreams/72f6a139-8919-4423-b5ee-7954b48c9c83/content

[11] S. Damodara, S. Shahriari, W.-I. Wu, P. Rezai, H.-H. Hsu, and R. Selvaganapathy, “Materials and methods for microfabrication of microfluidic devices,” in *Microfluidic Devices for Biomedical Applications*, Elsevier, 2021, pp. 1–78. doi: 10.1016/B978-0-12-819971-8.00008-1.

[12] Bruus, Henrik, “Theoretical microfluidics.” Accessed: Mar. 22, 2024. [Online]. Available: https://homes.nano.aau.dk/lg/Lab-on-Chip2008_files/HenrikBruus_Microfluidics%20lectures.pdf

[13] N. Lee-Yow, K. L. Pitts, and M. Fenech, “Optically clear biomicroviscometer with modular geometry using disposable PDMS chips,” in *2017 IEEE International Symposium on Medical Measurements and Applications (MeMeA)*, Rochester, MN, USA: IEEE, May 2017, pp. 72–77. doi: 10.1109/MeMeA.2017.7985852.

[14] H. Oertel, *Biofluid Mechanics*, vol. 158. 2010. doi: 10.1007/978-1-4419-1564-1_12.

[15] K. S. Lee and R. J. Ram, “Plastic-PDMS bonding for high pressure hydrolytically stable active microfluidics,” *Lab Chip*, vol. 9, pp. 1618–1624, 2009, doi: 10.1039/b820924c.

[16] B. Chayer, K. L. Pitts, G. Cloutier, and M. Fenech, “Velocity measurement accuracy in optical microhemodynamics: experiment and simulation,” *Physiol. Meas.*, vol. 33, no. 10, p. 1585, Sep. 2012, doi: 10.1088/0967-3334/33/10/1585.

[17] R. Mehri, C. Mavriplis, and M. Fenech, “Design of a microfluidic system for red blood cell aggregation investigation,” *J. Biomech. Eng.*, vol. 136, no. 6, Jun. 2014, doi: 10.1115/1.4027351/440223.

[18] K. L. Pitts and M. Fenech, “Micro-particle Image Velocimetry for Velocity Profile Measurements of Micro Blood Flows,” *J. Vis. Exp. JoVE*, no. 74, p. e50314, 2013, doi: 10.3791/50314.

[19] D. J. Beebe, G. A. Mensing, and G. M. Walker, “Physics and Applications of Microfluidics in Biology,” *Annu. Rev. Og Biomed. Eng.*, vol. 4, 2002, Accessed: Oct. 18, 2023. [Online]. Available: https://www-annualreviews-org.proxy.bib.uottawa.ca/doi/10.1146/annurev.bioeng.4.112601.125916

[20] J. El-Ali, P. K. Sorger, and K. F. Jensen, “Cells on chips,” *Nature*, vol. 442, no. 7101, pp. 403–411, Jul. 2006, doi: 10.1038/nature05063.

[21] T. Betancourt and L. Brannon-Peppas, “Micro- and nanofabrication methods in nanotechnological medical and pharmaceutical devices,” *Int. J. Nanomedicine*, vol. 1, no. 4, pp. 483–495, Dec. 2006.

[22] Y. Xia and G. M. Whitesides, “SOFT LITHOGRAPHY,” *Annual Review of Materials Research*, vol. 28, no. Volume 28, 1998. Annual Reviews, pp. 153–184, 1998. doi: https://doi.org/10.1146/annurev.matsci.28.1.153.

[23] M. W. Toepke and D. J. Beebe, “PDMS absorption of small molecules and consequences in microfluidic applications,” *Lab. Chip*, pp. 1484–1486, 2006, doi: 10.1039/b612140c.

[24] J. C. McDonald and G. M. Whitesides, “Poly(dimethylsiloxane) as a Material for Fabricating Microfluidic Devices,” *ChemInform*, vol. 33, no. 38, pp. 265–265, Sep. 2002, doi: 10.1002/CHIN.200238265.

[25] B. S. Hardy, K. Uechi, J. Zhen, and H. P. Kavehpour, “The deformation of flexible PDMS microchannels under a pressure driven flow,” *Lab. Chip*, vol. 9, no. 7, pp. 935–938, Apr. 2009, doi: 10.1039/B813061B.

[26] T. Gervais, J. El-Ali, A. Günther, and K. F. Jensen, “Flow-induced deformation of shallow microfluidic channels,” *Lab Chip*, vol. 6, pp. 500–507, 2006, doi: 10.1039/b513524a.

[27] M. Liu, J. Sun, Y. Sun, C. Bock, and Q. Chen, “Thickness-dependent mechanical properties of polydimethylsiloxane membranes,” *J. Micromechanics Microengineering*, vol. 19, no. 3, Feb. 2009, doi: 10.1088/0960-1317/19/3/035028.

[28] E. P. Dupont, R. Luisier, and M. A. M. Gijs, “NOA 63 as a UV-curable material for fabrication of microfluidic channels with native hydrophilicity,” *Microelectron. Eng.*, pp. 1253–1255, 2010, doi: 10.1016/j.mee.2009.11.084.

[29] E. Sollier, C. Murray, P. Maoddi, and D. D. Carlo, “Rapid prototyping polymers for microfluidic devices and high pressure injections †,” *Lab Chip*, vol. 11, pp. 3752–3765, 2011, doi: 10.1039/c1lc20514e.

[30] E. Marieb and K. Hoehn, *Anatomie et physiologie humaines*.

[31] R. J. Laird and S. Irwin, *Cardiovascular Structure and Function*. 2004. doi: 10.1016/B978-032301840-1.50005-0.

[32] G. Guven, M. P. Hilty, and C. Ince, “Microcirculation: Physiology, Pathophysiology, and Clinical Application,” *Blood Purif.*, vol. 49, no. 1–2, pp. 143–150, 2020, doi: 10.1159/000503775.

[33] J. E. Hall and A. C. Guyton, *Guyton and Hall Textbook of Medical Physiology*, 12th ed. Philadelphia, Pa: Saunders/Elsevier, 2011.

[34] S. Eriksson, J. Nilsson, and C. Sturesson, “Non-invasive imaging of microcirculation: a technology review,” *Med. Devices Auckl. NZ*, vol. 7, pp. 445–452, Dec. 2014, doi: 10.2147/MDER.S51426.

[35] D. A. Bottino and E. Bouskela, “Non-invasive techniques to access in vivo the skin microcirculation in patients,” *Front. Med.*, vol. 9, 2023, Accessed: Oct. 16, 2023. [Online]. Available: https://www.frontiersin.org/articles/10.3389/fmed.2022.1099107

[36] A. Girach and R. C. Sergott, *Optical Coherence Tomography*. Springer International Publishing, 2016. Accessed: Mar. 12, 2024. [Online]. Available: https://books-scholarsportal-info.proxy.bib.uottawa.ca/en/read?id=/ebooks/ebooks3/springer/2017-08-17/2/9783319248172#page=1

[37] Britannica, The Editors of Encyclopaedia, “Capillary | Blood Vessels, Exchange & Function | Britannica,” Encyclopedia Britannica. Accessed: Mar. 10, 2024. [Online]. Available: https://www.britannica.com/science/capillary

[38] L. Julien, S. Bonnin, M. Paques, and J.-M. Fullana, “One-dimensional modeling of microvascular hemodynamics in the retina using multimodal imaging,” *Phys. Fluids*, vol. 35, no. 6, p. 061901, Jun. 2023, doi: 10.1063/5.0152499.

[39] G. Guidoboni *et al.*, “Neurodegenerative Disorders of the Eye and of the Brain: A Perspective on Their Fluid-Dynamical Connections and the Potential of Mechanism-Driven Modeling,” *Front. Neurosci.*, vol. 14, p. 566428, 2020, doi: 10.3389/fnins.2020.566428.

[40] A. V. Stanton *et al.*, “Vascular network changes in the retina with age and hypertension,” *J. Hypertens.*, vol. 13, no. 12 Pt 2, pp. 1724–1728, Dec. 1995.

[41] T. Y. Wong, R. Klein, B. E. K. Klein, J. M. Tielsch, L. Hubbard, and F. J. Nieto, “Retinal Microvascular Abnormalities and their Relationship with Hypertension, Cardiovascular Disease, and Mortality,” *Surv. Ophthalmol.*, vol. 46, no. 1, pp. 59–80, Jul. 2001, doi: 10.1016/S0039-6257(01)00234-X.

[42] M. Paques, “Systolodiastolic variations of blood flow during central retinal vein occlusion: exploration by dynamic angiography,” *Br. J. Ophthalmol.*, vol. 89, no. 8, pp. 1036–1040, Aug. 2005, doi: 10.1136/bjo.2004.061275.

[43] D. A. Rubenstein, W. Yin, and M. D. Frame, “Chapter 2 - Fundamentals of Fluid Mechanics,” in *Biofluid Mechanics (Second Edition)*, D. A. Rubenstein, W. Yin, and M. D. Frame, Eds., in Biomedical Engineering. , Boston: Academic Press, 2015, pp. 15–62. doi: 10.1016/B978-0-12-800944-4.00002-0.

[44] Neutrium, “Viscosity | Neutrium,” Neutrium. Accessed: Mar. 12, 2024. [Online]. Available: https://neutrium.net/fluid-flow/viscosity/

[45] F. Pizzarelli, “Paired Hemodiafiltration,” in *Contributions to Nephrology*, C. Ronco, B. Canaud, and P. Aljama, Eds., Basel: KARGER, 2007, pp. 131–137. doi: 10.1159/000107243.

[46] R. Zhang, C. Y. Zhang, Q. Zhao, and D. H. Li, “Spectrin: Structure, function and disease,” *Sci. China Life Sci.*, vol. 56, no. 12, pp. 1076–1085, 2013, doi: 10.1007/s11427-013-4575-0.

[47] J. Dunn and M. H. Grider, “Physiology, Adenosine Triphosphate,” *StatPearls Publ.*, Feb. 2021, [Online]. Available: https://www.mendeley.com/reference-manager/library/all-references

[48] D. A. Fedosov, M. Peltomäki, and G. Gompper, “Deformation and dynamics of red blood cells in flow through cylindrical microchannels,” *Soft Matter*, vol. 10, no. 24, pp. 4258–4267, 2014, doi: 10.1039/C4SM00248B.

[49] C. Pfafferott, G. B. Nash, and H. J. Meiselman, “Red blood cell deformation in shear flow. Effects of internal and external phase viscosity and of in vivo aging,” *Biophys. J.*, vol. 47, no. 5, pp. 695–704, 1985, doi: 10.1016/S0006-3495(85)83966-7.

[50] G. Tomaiuolo, “Biomechanical properties of red blood cells in health and disease towards microfluidics,” *Biomicrofluidics*, vol. 8, no. 5, pp. 1–19, 2014, doi: 10.1063/1.4895755.

[51] L. Da Costa, J. Galimand, O. Fenneteau, and N. Mohandas, “Hereditary spherocytosis, elliptocytosis, and other red cell membrane disorders,” *Blood Rev.*, vol. 27, no. 4, pp. 167–178, Jul. 2013, doi: 10.1016/j.blre.2013.04.003.

[52] A. Semenov, A. Lugovtsov, P. Ermolinskiy, K. Lee, and A. Priezzhev, “Problems of Red Blood Cell Aggregation and Deformation Assessed by Laser Tweezers, Diffuse Light Scattering and Laser Diffractometry,” *Photonics*, vol. 9, no. 4, Art. no. 4, Apr. 2022, doi: 10.3390/photonics9040238.

[53] N. L. Parrow *et al.*, “Measuring Deformability and Red Cell Heterogeneity in Blood by Ektacytometry,” *J. Vis. Exp. JoVE*, no. 131, p. 56910, Jan. 2018, doi: 10.3791/56910.

[54] S. Yu. Nikitin, A. V. Priezzhev, and A. E. Lugovtsov, “Analysis of laser beam scattering by an ensemble of particles modeling red blood cells in ektacytometer,” *J. Quant. Spectrosc. Radiat. Transf.*, vol. 121, pp. 1–8, May 2013, doi: 10.1016/j.jqsrt.2013.02.014.

[55] I. Safeukui *et al.*, “Sensing of red blood cells with decreased membrane deformability by the human spleen,” *Blood Adv.*, vol. 2, no. 20, pp. 2581–2587, Oct. 2018, doi: 10.1182/bloodadvances.2018024562.

[56] R. Mehri, C. Mavriplis, and M. Fenech, “Red blood cell aggregates and their effect on non-Newtonian blood viscosity at low hematocrit in a two-fluid low shear rate microfluidic system,” *PLoS ONE*, vol. 13, no. 7, 2018, doi: 10.1371/journal.pone.0199911.

[57] O. Baskurt, B. Neu, and H. J. Meiselman, “Red blood cell aggregation,” *Red Blood Cell Aggreg.*, pp. 1–288, 2011, doi: 10.1201/b11221.

[58] D. A. Fedosov, B. Caswell, A. S. Popel, and G. E. M. Karniadakis, “Blood Flow and Cell-Free Layer in Microvessels,” *Microcirculation*, vol. 17, no. 8, pp. 615–628, 2010, doi: 10.1111/j.1549-8719.2010.00056.x.

[59] C. Delong and S. Sharma, “Physiology, Peripheral Vascular Resistance,” in *StatPearls*, Treasure Island (FL): StatPearls Publishing, 2024. Accessed: Mar. 10, 2024. [Online]. Available: http://www.ncbi.nlm.nih.gov/books/NBK538308/

[60] D. Mohrman, “Central Venous Pressure: An Indicator of Circulatory Hemodynamics,” in *Cardiovascular Physiology*, 7th ed., The McGraw-Hill Companies, 2010, pp. 148–162.

[61] T. G. Papaioannou *et al.*, “Total arterial compliance estimated by a novel method and all-cause mortality in the elderly: The PROTEGER study,” *Age*, vol. 36, no. 3, pp. 1555–1563, 2014, doi: 10.1007/s11357-014-9661-0.

[62] L. Julien, “Microvascular network of the retina: 1D-model, microfluidic device and high resolution data,” Thesis, Sorbonne University, Paris, France, 2024. [Online]. Available: https://theses.fr/2023SORUS719

[63] MicroChem, “NANO SU-8 2000 Negative Tone Photoresist Formulations 2035-2100,” pp. 1–4, 2011.

[64] Y. J. Chuang, F. G. Tseng, and W. K. Lin, “Reduction of diffraction effect of UV exposure on SU-8 negative thick photoresist by air gap elimination,” *Microsyst. Technol.*, vol. 8, no. 4–5, pp. 308–313, Aug. 2002, doi: 10.1007/S00542-002-0176-8/METRICS.

[65] M. Fenech, V. Girod, V. Claveria, S. Meance, M. Abkarian, and B. Charlot, “Microfluidic blood vasculature replicas using backside lithography,” *Lab. Chip*, vol. 19, no. 12, pp. 2096–2106, Jun. 2019, doi: 10.1039/C9LC00254E.

[66] J. H. Sim, H. J. Moon, Y. H. Roh, H. W. Jung, and K. W. Bong, “Fabrication of NOA microfluidic devices based on sequential replica molding,” *Korean J. Chem. Eng.*, vol. 34, no. 5, pp. 1495–1499, May 2017, doi: 10.1007/S11814-017-0041-1/METRICS.

[67] G. Zhuang and J. P. Kutter, “Anti-stiction coating of PDMS moulds for rapid microchannel fabrication by double replica moulding,” *J. Micromechanics Microengineering*, vol. 21, no. 10, p. 105020, Sep. 2011, doi: 10.1088/0960-1317/21/10/105020.

[68] K. Khanafer, A. Duprey, M. Schlicht, and R. Berguer, “Effects of strain rate, mixing ratio, and stress-strain definition on the mechanical behavior of the polydimethylsiloxane (PDMS) material as related to its biological applications,” *Biomed. Microdevices*, vol. 11, no. 2, pp. 503–508, Dec. 2009, doi: 10.1007/S10544-008-9256-6/FIGURES/8.

[69] X. Ye, H. Liu, Y. Ding, H. Li, and B. Lu, “Research on the cast molding process for high quality PDMS molds,” *Microelectron. Eng.*, vol. 86, pp. 310–313, 2009, doi: 10.1016/j.mee.2008.10.011.

[70] I. D. Johnston, D. K. McCluskey, C. K. L. Tan, and M. C. Tracey, “Mechanical characterization of bulk Sylgard 184 for microfluidics and microengineering,” *J. Micromechanics Microengineering*, vol. 24, no. 3, p. 035017, Feb. 2014, doi: 10.1088/0960-1317/24/3/035017.

[71] Sympatec, “Particle Shape,” Sympatec. Accessed: May 03, 2024. [Online]. Available: https://www.sympatec.com/en/particle-measurement/glossary/particle-shape/

[72] D. Wang and L.-S. Fan, “2 - Particle characterization and behavior relevant to fluidized bed combustion and gasification systems,” in *Fluidized Bed Technologies for Near-Zero Emission Combustion and Gasification*, F. Scala, Ed., in Woodhead Publishing Series in Energy. , Woodhead Publishing, 2013, pp. 42–76. doi: 10.1533/9780857098801.1.42.

[73] O. K. Baskurt and H. J. Meiselman, “Data reduction methods for ektacytometry in clinical hemorheology,” *Clin. Hemorheol. Microcirc.*, vol. 54, no. 1, pp. 99–107, May 2013, doi: 10.3233/CH-2012-1616.

[74] S. Tavoularis, “Measurement in Fluid Mechanics,” *J. Fluids Struct. 23*, pp. 159–160, 2007, doi: 10.1016/j.jfluidstructs.2006.08.003.

[75] Norland Products, “Norland Optical Adhesive 63,” Norland Products. Accessed: Oct. 20, 2023. [Online]. Available: https://www.norlandprod.com/adhesives/noa%2063.html

[76] I. Sotiri *et al.*, “Tunability of liquid-infused silicone materials for biointerfaces,” *Biointerphases*, vol. 13, p. 06D401, Dec. 2018, doi: 10.1116/1.5039514.

[77] L. Gitlin, P. Schulze, and D. Belder, “Rapid replication of master structures by double casting with PDMS,” *Lab. Chip*, vol. 9, no. 20, pp. 3000–3002, Oct. 2009, doi: 10.1039/B904684D.

[78] S. Xie, J. Wu, B. Tang, G. Zhou, M. Jin, and L. Shui, “Large-Area and High-Throughput PDMS Microfluidic Chip Fabrication Assisted by Vacuum Airbag Laminator,” *Micromachines 2017 Vol 8 Page 218*, vol. 8, no. 7, p. 218, Jul. 2017, doi: 10.3390/MI8070218.

[79] C. Kang, C. Roh, and R. A. Overfelt, “Pressure-driven deformation with soft polydimethylsiloxane (PDMS) by a regular syringe pump: challenge to the classical fluid dynamics by comparison of experimental and theoretical results,” *RSC Adv.*, vol. 4, no. 7, pp. 3102–3112, Dec. 2014, doi: 10.1039/C3RA46708B.

[80] H. Park *et al.*, “Measuring cell surface area and deformability of individual human red blood cells over blood storage using quantitative phase imaging,” *Sci. Rep.*, vol. 6, p. 34257, Oct. 2016, doi: 10.1038/srep34257.

[81] A. M. Forsyth, J. Wan, W. D. Ristenpart, and H. A. Stone, “The dynamic behavior of chemically ‘stiffened’ red blood cells in microchannel flows,” *Microvasc. Res.*, vol. 80, no. 1, pp. 37–43, Jul. 2010, doi: 10.1016/j.mvr.2010.03.008.

[82] N. Z. Piety, J. Stutz, N. Yilmaz, H. Xia, T. Yoshida, and S. S. Shevkoplyas, “Microfluidic capillary networks are more sensitive than ektacytometry to the decline of red blood cell deformability induced by storage,” *Sci. Rep.*, vol. 11, no. 1, p. 604, Jan. 2021, doi: 10.1038/s41598-020-79710-3.

[83] P. N. Shankar and M. Kumar, “Experimental determination of the kinematic viscosity of glycerol-water mixtures,” *R. Soc.*, vol. 444, no. 1922, pp. 573–581, Mar. 1994, doi: 10.1098/rspa.1994.0039.

[84] K. Takamura, H. Fischer, and N. R. Morrow, “Physical properties of aqueous glycerol solutions,” *J. Pet. Sci. Eng.*, vol. 98–99, pp. 50–60, Nov. 2012, doi: 10.1016/j.petrol.2012.09.003.

[85] K. L. Pitts, S. Abu-Mallouh, and M. Fenech, “Contact angle study of blood dilutions on common microchip materials,” *J. Mech. Behav. Biomed. Mater.*, vol. 17, pp. 333–336, Jan. 2013, doi: 10.1016/J.JMBBM.2012.07.007.

[86] Z. Li, S. Y. Mak, A. Sauret, and H. C. Shum, “Syringe-pump-induced fluctuation in all-aqueous microfluidic system implications for flow rate accuracy †,” *Lab Chip*, vol. 14, p. 744, 2014, doi: 10.1039/c3lc51176f.

[87] W. Zeng, I. Jacobi, D. J. Beck, S. Li, and H. A. Stone, “Characterization of syringe-pump-driven induced pressure fluctuations in elastic microchannels,” *Lab Chip*, vol. 15, p. 1110, 2014, doi: 10.1039/c4lc01347f.